water

MDPI

Article

Study on the Transient Flow Characteristics of Multistage Centrifugal Pumps during the Startup Process before System Operation

Chao Chen [1], Hu Xu [1], Fanjie Deng [1], Kaipeng Wu [1], Zhen Zhang [2] and Qiaorui Si [1,*]

[1] National Research Centre of Pumps, Jiangsu University, Zhenjiang 212013, China; chch3605@ujs.edu.cn (C.C.); xuhuujs@163.com (H.X.); dengfanjie@foxmail.com (F.D.); 13673377383@163.com (K.W.)
[2] Jiangsu Branch of China Academy of Machinery Science and Technology Group Co., Ltd., Changzhou 213164, China; 18910135695@163.com
* Correspondence: siqiaorui@ujs.edu.cn; Tel.: +86-136-5529-3881

Abstract: Multistage pumps are essential in emergency water supply, irrigation, and other systems undergoing unavoidable hydraulic transitions like pump startup and valve operations. These transitions cause rapid changes in impeller speed, flow rate, and pressure, destabilizing the internal flow field and impacting system reliability. To study transient flow characteristics, a numerical analysis of a three-stage pump was conducted, focusing on vortex identification, entropy production, and time–frequency pressure pulsation. Using the SST turbulence model, the simulation analyzed different start times and flow rate variations. Findings revealed that shorter startup times intensified transient effects, with the head increasing rapidly initially and then stabilizing. Vortex structures showed periodic development and dissipation. Entropy production rose with impeller speed, peaking higher with shorter startups. Blade passing frequency dominated pressure pulsations, with increased low-frequency pulsations as speed rose. During valve opening, flow stabilization accelerated with increasing flow rates, reducing amplitude and eliminating low-frequency components. This research aids the reliable operation of high-pressure pumping systems in energy storage.

Keywords: multistage centrifugal pump; startup process; transient characteristics; flow vortex; entropy production; pressure pulsation

check for updates

Citation: Chen, C.; Xu, H.; Deng, F.; Wu, K.; Zhang, Z.; Si, Q. Study on the Transient Flow Characteristics of Multistage Centrifugal Pumps during the Startup Process before System Operation. *Water* **2024**, *16*, 1876. https://doi.org/10.3390/w16131876

Academic Editor: Bommanna Krishnappan

Received: 27 May 2024
Revised: 27 June 2024
Accepted: 28 June 2024
Published: 29 June 2024

1. Introduction

Multistage pumps are extensively applied in various water supply systems, including emergency water supply and irrigation. Their design allows for high efficiency and reliability, making them suitable for scenarios requiring consistent and high-pressure water delivery. The ability to handle a wide range of flow rates and heads makes multistage pumps a versatile solution for ensuring the availability of water in critical applications. Multistage pumps are a crucial component in emergency water supply, irrigation, and other water supply systems. Their stability and reliability directly impact the operational efficiency of these systems and the safety of water supply projects. The startup process before pump operation generally goes through two stages: increasing the speed and opening the valve, accompanied by unstable hydraulic characteristics. The transient flow inside the pump leads to these instability phenomena, which can threaten the system's reliability. Further research in this area is warranted [1–3].

Currently, the research on transient flow in hydraulic machinery during transitional processes primarily involves three aspects: theoretical research, numerical simulation, and experimental analysis. Theoretical research provides fundamental support for understanding fluid properties and flow behavior changes. In terms of theoretical research, Li et al. [4] employed a dynamic mesh method combined with a dynamic slip zone method to create a physical model of a pipeline system and pump, focusing on the rotational speed of the flow field around the impeller. Wang et al. [5] introduced an optimization method to minimize pump start and stop times using the storm water management model (SWMM) and particle swarm optimization (PSO). Liu et al. [6] proposed a time-step algorithm to predict the transient performance of pumps under rapid startup conditions and studied mixed-flow pumps under different acceleration times. Li et al. [7] developed a theoretical prediction model based on transient head and pipeline resistance balance, conducting both experimental and theoretical studies on the transient performance of a centrifugal pump under linear acceleration start conditions. Kan et al. [8] utilized bidirectional fluid–structure interaction to simulate the flow field of an axial flow pump and designed a method to increase blade strength without impacting hydraulic performance while also validating their simulation results through experimental methods for measuring dynamic stress of hydraulic machinery underwater.

Numerical simulation can utilize computers to address complex flow problems. In terms of numerical simulation, Ren et al. [9] studied the effects of different speed control startup methods on mixed-flow pumps. They focused on addressing issues such as head impact, tip leakage vortex, and pressure pulsation during pump startup to minimize vibration and noise. Fu et al. [10] conducted experimental and numerical investigations on transient characteristics of axial flow pumps during startup, examining their impact on system load and fluid pressure. Kan et al. [11] used the entropy production method to identify energy loss areas in bidirectional axial flow pumps during transition processes. Yang et al. [12] examined the flow patterns and pressure pulsation evolution in a prototype pump–turbine during transitional processes through 1D and 3D computational fluid dynamics (CFD) simulations. Yun et al. [13] conducted numerical simulations to analyze the startup process of multistage centrifugal pumps during valve transitions and studied the pump's characteristics and internal flow field evolution.

Experimental analysis can offer real and reliable data to support research outcomes. In the area of experimental analysis, Lu et al. [14] used an experimental system to measure cavitation and vibration in the pump during steady-state and rapid startup processes, finding a strong correlation between cavitation and vibration. Zhu et al. [15] collected data on noise, shaft vibration, and pressure pulsation under linear and nonlinear startup modes, observing high amplitude sound pressure in the later stages of startup. Tang et al. [16] analyzed the impact of startup mode on the stability of a mixed-flow pump, finding a positive correlation between impeller acceleration and external characteristic parameters. Li et al. [17] investigated the transient flow characteristics during the startup process of a pump–pipe system, finding that pressure impact could be mitigated by adjusting the air volume ratio or valve opening time. Abdulkhaev et al. [18] studied the hydraulic shock process during centrifugal pump startup, emphasizing the importance of selecting parameters for improving the system reliability.

To sum up, the research works on the hydraulic transition characteristic of single-stage centrifugal pump units during the starting and stopping process has been developed maturely, but due to the complex structure parameters, repeated structural and mesh adjustment, the reliable numerical transient simulation methods for low specific speed multistage centrifugal pumps have not been developed substantially. Therefore, a modified shear stress transport (SST) turbulence model, together with programming functions for controlling variation in impeller rotational speed and flow rate, are developed to calculate the transient and turbulent inner flow of a three-stage model pump in this study. Data from various hydraulic perspectives, such as pump performance, vortex structure, entropy generation, and pressure pulsation, the changing characteristics of important performance parameters during the startup process, including increasing the impeller rotational speed and opening the outlet valve process, are revealed.

2. Experimental Model and Computational Method

2.1. Pump Parameters and Computational Domain

The segmented multistage pumps are taken as the research object with a three-stage pump. As illustrated in Table 1, the design rotational speed of the pump is 3800 r/min, and the single-stage specific speed of the pump is 41.6. The computational domain includes the inlet, suction chamber, volute, pump chamber, impeller, guide vane, impeller ring, and outlet. In order to reduce the influence of the positions of the inlet and outlet on the internal flow of the pump, the length of the inlet and outlet sections is set to 5 times the diameter of the pump. The calculation domain of the three-stage centrifugal pump is shown in Figure 1.

Table 1. Main parameters of the three-stage pump.

Parameter	Value
Rotational speed, n	3800 r/min
Flow rate, Q_d	36.0 m^3/h
Single-stage head, H	107.1 m
Specific speed, n_s	41.6
Number of impeller blades, Z	5
Number of guide vane blades, Z_d	4
Pump inlet diameter, D_1	80 mm
Pump outlet diameter, D_2	65 mm

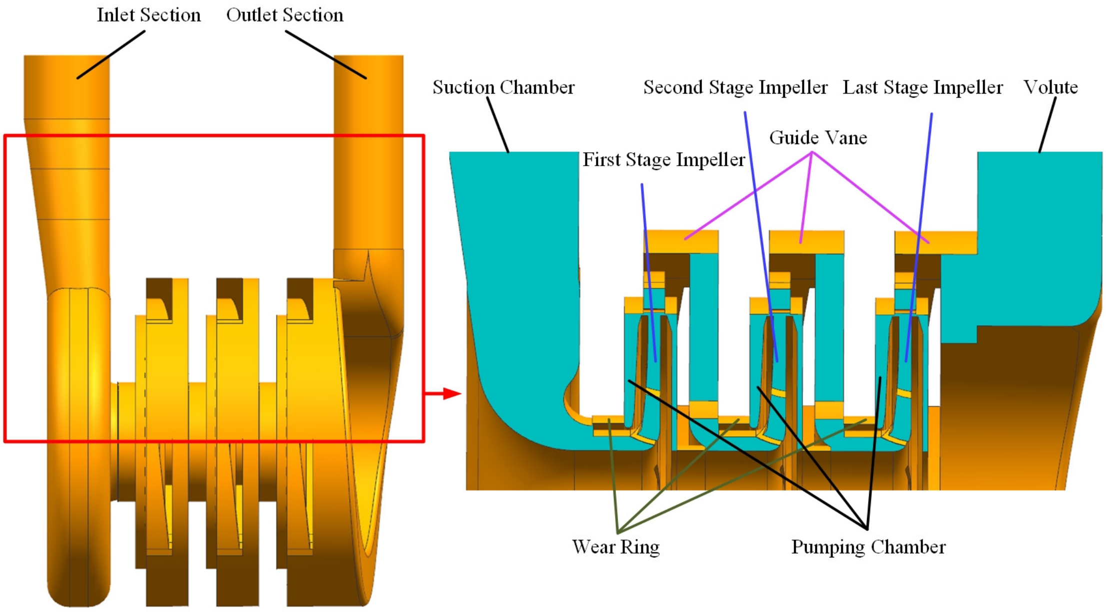

Figure 1. Calculation domain of three-stage centrifugal pump.

In order to improve simulation accuracy and accelerate convergence speed, a hybrid meshing technique is employed to build the computational domain. The hybrid mesh combines structured and unstructured grids, which allows for adaptability to complex geometries while maintaining computational efficiency and accuracy. Different regions within the computational domain water body, such as the inlet and outlet, impeller ring, impeller, and guide vanes, have relatively simple structures and are meshed using hexahedral structured grids. On the other hand, the suction chamber, pump chamber, and volute, which have more complex structures, are meshed using tetrahedral unstructured grids, which are better suited for such geometries.

To ensure the accuracy of numerical simulations and reduce computational resource consumption, five sets of grids with different mesh quantities are used to numerically simulate and analyze the fluctuation changes of heads under various operating conditions.

The numerical results of the head variation are presented in Table 2. It can be observed from the table that when the number of grids exceeds 14.2 million, with an increasing number of grids, the variation in the head becomes relatively small and tends to stabilize. Additionally, the relative error of the head is less than 0.02%. To ensure computational accuracy without excessive cost, an overall grid number of 14.2 million with grid quality above 0.3 was selected. To improve the precision in capturing flow changes near the blade surface, a first-layer grid height of 0.015 mm and a grid growth rate of 1.5 were established. The value of Y+ (dimensionless wall distance) on the blade surface is maintained below 30 to meet the requirements of the turbulence model. The mesh of the impeller and the Y+ distribution on the blade surface is shown in Figure 2.

Table 2. Grid independence analysis.

Number	The Number of Mesh/Million	Head/m	Relative Error/%
1	1.273×10^7	337.25	-
2	1.342×10^7	340.61	1
3	1.420×10^7	342.79	0.64
4	1.487×10^7	342.87	0.02
5	1.549×10^7	342.92	0.015

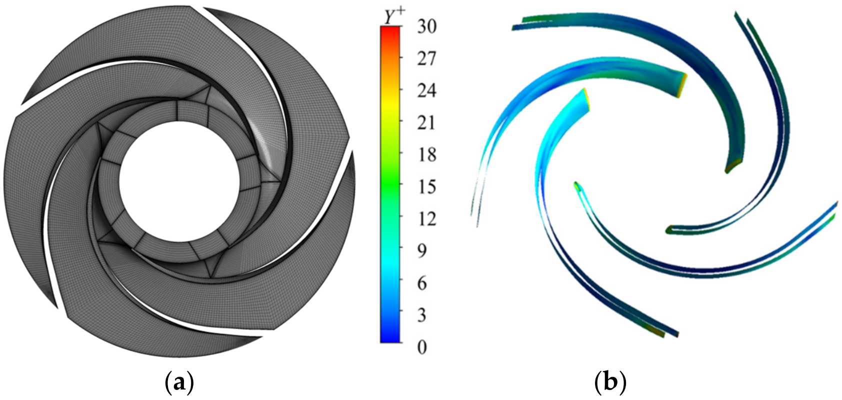

(**a**) (**b**)

Figure 2. Details of grids: (**a**) emergency water supply multistage pump impeller grid and (**b**) distribution of Y plus on the blade surface.

2.2. Computational Simulation Method

2.2.1. Equations and Turbulent Model

The shear stress transport (SST) model is currently one of the most widely employed Reynolds-averaged Navier–Stokes (RANS) models within the realm of Turbulence modeling, and it is recognized for its superior performance in evaluating turbulent flows [19]. The standard SST turbulence model models Reynolds stresses as isotropic, rendering it insensitive to directional forces and, in turn, neglecting the influence of certain other behaviors [20].

During the startup of a pump, the flow experiences high turbulence due to acceleration effects and is simultaneously significantly affected by curvature effects. The macroscopic manifestation of curvature effects on turbulence within the flow can either enhance or suppress turbulence intensity, i.e., promote or inhibit the production of turbulent kinetic energy (k). This implies that within the fundamental framework of the SST model, this influence can be coupled to the transport equations of k and ω through specific methodologies while the model structure remains unaltered [21].

Smirnov and Menter [22] added a correction to the production term in the k and ω equation within the shear stress transport (SST) k-ω model. This adjustment, known as the SST-CC (curvature correction) model, was introduced to improve the accuracy of the model:

$$\frac{\partial k}{\partial t} + \frac{\partial \langle u \rangle_i k}{\partial x_i} = f_{r1} P_k + \frac{\partial}{\partial x_i}\left[(v + v_t)\frac{\partial k}{\partial x_i}\right] - \beta^* k\omega \tag{1}$$

$$\frac{\partial \omega}{\partial t} + \frac{\partial \langle u \rangle_i \omega}{\partial x_i} = \frac{\alpha f_{r1} P_k}{v_t} + \frac{\partial}{\partial x_i}\left[(v + v_t)\frac{\partial \omega}{\partial x_i}\right] - D_\omega + Cd_\omega \tag{2}$$

The production of turbulent kinetic energy (P_k) and other parameters can be found in reference [22]. Additionally, a multiplier known as the "rotation function" has been introduced:

$$f_r = (1 + c_{r1})\frac{2r^*}{1 + r^*}\left[1 - c_{r3}\ \tan^{-1}(c_{r2}\tilde{r})\right] - c_{r1} \tag{3}$$

Unlike the original proposal, the rotation function is restricted as follows:

$$f_{r1} = \max\{\min(f_r, 1.25), 0\} \tag{4}$$

The value of 1.25 for the limiter indicates strong convex curvature and is an empirical constant. The introduction of the lower limiter at 0 is for maintaining numerical stability.

The effect of rotation/curvature can be achieved by parameterizing model constants to suppress or increase the growth rate of turbulent kinetic energy or by parameterizing the eddy viscosity coefficient to achieve curvature effects [23].

2.2.2. Boundary Conditions and Controlling Functions

This study uses pure water with the SST-CC turbulence model. The initial file for unsteady calculations during startup with the valve fully closed is a steady-state flow field with zero rotational speed. The inlet boundary condition is set as total pressure inlet with a value of 101,325 Pa, and the outlet boundary condition is set as a mass flow rate outlet. The impeller region is defined as a rotating domain, with other regions as stationary domains and wall boundary conditions set as no-slip walls. The grid nodes are treated using the general grid interface (GGI) mode. The frozen rotor method is used for steady-state calculations for dynamic–static coupling interfaces and the transient rotor–stator method is used for unsteady calculations. The time step is set to 0.001 s, with a maximum of 15 iterations per time step. The convergence criterion is set as the maximum residual being less than 1×10^{-4}.

During the startup process, it is generally assumed that the flow rate is 0. However, in reality, there still exists a small flow circulation inside the multistage centrifugal pump, which is close to the impeller ring leakage flow and is approximately 1% to 5% of the pump's design flow rate. In this paper, a mass flow rate of 0.0997 kg/s is selected.

The rotational speed variation during the startup process is approximated to be linear. The rotational speed variation is as follows:

$$n = n_f \times (r/T) \tag{5}$$

where n is the rotational speed at the corresponding time, r/min, n_f is the operational rotational speed after the completion of the startup process, r/min, t is the current time during the startup process, s, and T is the total time taken for the startup acceleration, s.

Take the flow field at the impeller rotational speed of 3800 r/min as the initial state for the valve opening process calculation. Set two types of flow rate variation patterns, separately linear and exponential, to simulate the valve opening pattern. The control expression for the linear flow rate variation pattern is as follows:

$$Q = Q_d \times (t/T) \tag{6}$$

where Q is the flow rate at the corresponding time, $\mathrm{m^3/h}$, Q_d is the design flow rate of the multistage pump, $\mathrm{m^3/h}$, and T is the total time of flow change, s.

The control expression for the exponential flow rate variation pattern is as follows:

$$Q = Q_d - Q_d \times \exp(-t/t_0) \tag{7}$$

where t_0 is the nominal acceleration time of the flow rate, which is the time required from static to 63.2% of the design flow rate; 0.2 s is set in this calculation.

2.3. Computational Simulation Methods

2.3.1. Equation of Vortex Identification

In order to better explore the development of vortex structures inside the pump during startup, the new generation vortex identification method called the "Omega (Ω)" method was adopted to analyze the vortex structures. The new generation vortex identification method was proposed by Liu et al. [24] in 2016. Compared to other second-generation vortex identification methods, the Ω method has several advantages, such as easy implementation, normalization, the ability to capture both strong and weak vortices, and insensitivity to threshold values.

Liu et al. [25] divided the vorticity ($\vec{\omega}$) into two parts, the rotating part and the non-rotating part, and quoted a parameter to represent the ratio of the rotating vorticity to the total vorticity. The related equations can be described as follows:

$$\vec{\omega} = \vec{R} + \vec{S} \tag{8}$$

$$\varepsilon = 0.001\left(\|A\|_F^2 + \|B\|_F^2\right)_{\max} \tag{9}$$

$$\Omega = \frac{\|B\|_F^2}{\|A\|_F^2 + \|B\|_F^2 + \varepsilon} \tag{10}$$

where $\vec{R}$ represents the vorticity of the rotating part, $\vec{S}$ represents the vorticity of the non-rotating part, and $\| \ \|_F$ represents the Frobenius norm of the matrix. In practical applications, a fixed value of $\Omega = 0.52$ is commonly adopted as the threshold for vortex detection.

2.3.2. Equation of the Entropy Generation

The entropy generation in a multistage pump refers to the irreversible energy loss caused by the presence of viscosity and Reynolds stress in the working fluid during the pump's operation, leading to the irreversible conversion of mechanical energy into internal energy [26]. According to the theory proposed by Kock [27], there is an inherent connection between the turbulent dissipation entropy production rate and the turbulence model, which is reflected by the turbulent dissipation rate ε. Therefore, in the SST k-ω turbulence model, we have the following expression:

$$\dot{S}'''_{D'} = \alpha\frac{\rho\omega k}{T} \tag{11}$$

The equation is as follows: α is an empirical coefficient with a value of 0.09, ω is turbulent fluctuation frequency, measured in $\mathrm{s^{-1}}$, and k is turbulent intensity, measured in $\mathrm{m^2/s^2}$.

However, the local entropy yield will have a more obvious wall effect, and the time-averaged term is more obvious, and its calculation formula is as follows:

$$\dot{S}''_{W} = \frac{\vec{\tau}\cdot\vec{v}}{T} \tag{12}$$

where $\vec{\tau}$ is wall shear stress, measured in Pascals (Pa), and $\vec{v}$ is the velocity at the first grid layer near the wall, measured in meters per second (m/s).

Integrating the volume of the local entropy yield domain and integrating the surface area of the wall entropy yield domain yields:

$$S_{pro,\overline{D}} = \int_V \dot{S}'''_{\overline{D}} dV \tag{13}$$

$$S_{pro,D'} = \int_V \dot{S}'''_{D'} dV \tag{14}$$

$$S_{pro,W} = \int_V \dot{S}''_{W} dS \tag{15}$$

where $S_{pro,\overline{D}}$ is the direct dissipation entropy production, W/K, $S_{pro,D'}$ is the turbulent dissipation entropy production, W/K, and $S_{pro,W}$ is the wall entropy production, W/K.

Therefore, the total entropy in the computational domain is as follows:

$$S_{pro} = S_{pro,\overline{D}} + S_{pro,D'} + S_{pro,W} \tag{16}$$

2.3.3. Pressure Pulsation Analysis

In order to study the pressure pulsation characteristics of the multistage pump during the startup process, the operating condition with a startup time of 1 s was selected. Pressure pulsation monitoring points were placed inside each stage's impeller and guide vanes. These points were denoted by letters A, B, and C, representing the first, second, and last stages of the multistage pump, respectively. Different areas within each stage were designated by combining letters and numbers to indicate the specific pressure pulsation monitoring points. Let us take the example of the arrangement of pressure pulsation monitoring points in the first stage, as shown in Figure 3. A1, A2, and A3 represent three pressure pulsation monitoring points within the impeller flow passage, and they move with the rotation of the impeller. A4, A5, and A6 represent three pressure pulsation monitoring points within the guide vane flow passage, and their positions remain fixed. The arrangement of pressure pulsation monitoring points in the second and last stages is the same as in the first stage, resulting in a total of 18 pressure pulsation monitoring points.

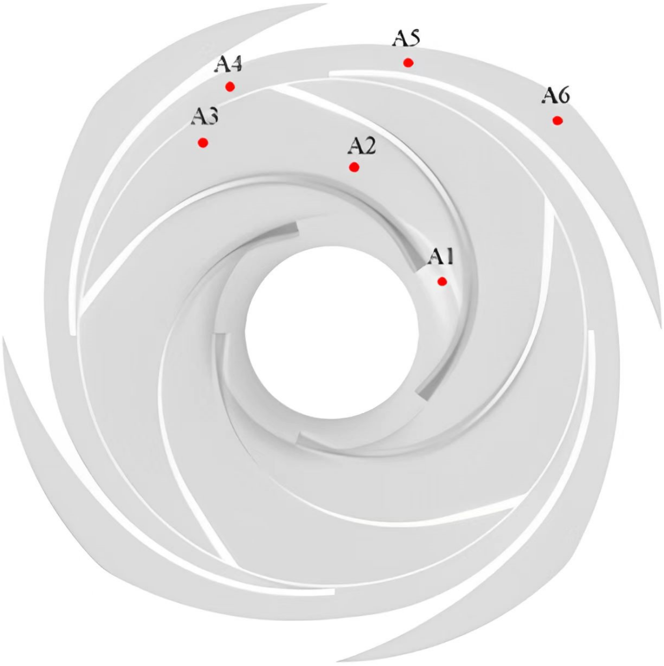

Figure 3. First-stage impeller monitoring point arrangement.

Due to the increase in pressure with the number of stages in the multistage centrifugal pump, in order to conveniently analyze the pressure pulsation variations within each stage, the pressure results can be made dimensionless. The pressure fluctuation coefficient, denoted as C_P, is used to characterize the fluctuation level of pressure pulsations. Its calculation formula is as follows:

$$C_P = \frac{P - \overline{P}}{0.5\rho u_2^2} \tag{17}$$

where P is the instantaneous pressure value at each monitoring point, Pa, $\overline{P}$ is the average instantaneous pressure value at each monitoring point, Pa, ρ is the density of the transported fluid, kg/m^3, and u_2 is the circumferential velocity at the impeller outlet, m/s.

2.4. Test Rig

In Figure 4, the performance tests of the multistage pump in both steady-state and startup processes were conducted on an open test bench in the pump test laboratory, following the ISO 9906:2012 standard [28]. The main equipment for the centrifugal pump unit performance test bench includes an electric control valve, electromagnetic flow meter, motor, static pressure sensor, dynamic pressure sensor, NI data acquisition card, and other devices. The accuracy of flow measurement is ±2.5%, head is ±3%, torque is ±2.5%, and rotation is ±1%. This experiment is based on controlling the start/stop and speed variations of the multistage pump by adjusting the start/stop and frequency settings of the variable frequency drive (VFD). The flow rate is regulated by an electric control valve located at the outlet of the multistage pump.

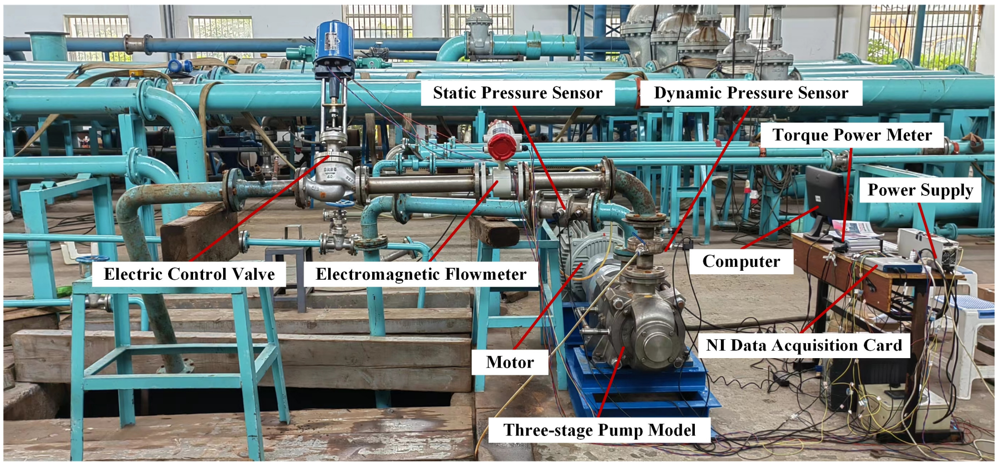

Figure 4. Centrifugal pump performance test bench.

3. Results Analysis

3.1. Experiment Validation

In order to obtain the performance variations of the multistage pump under different operating conditions, numerical calculations were performed for different operating speeds and different startup times. The reliability of the numerical simulation results was validated through experiments. As shown in Figure 5, it can be observed that the simulated trends of head and efficiency are similar to the experimental values. In most operating conditions, the simulated head is slightly lower than the experimental values, with a maximum relative error of 4.47%. On the other hand, the simulated efficiency is slightly higher than the experimental values, with a maximum relative error of 3.87%. Since the discrepancies between the simulated and experimental values of head and efficiency are within 5%, the accuracy and reliability of the model have been effectively validated.

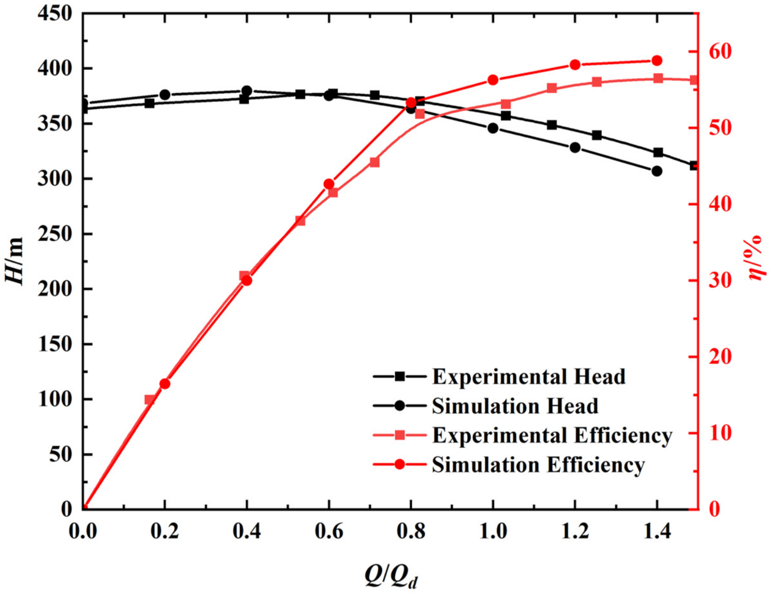

Figure 5. Comparison of performance of multistage pump.

Figure 6 shows the comparison between the simulated and experimental values of the performance during the startup process of the emergency water supply multistage pump at a specific rotational speed of 2900 r/min. The change in rotational speed during the test cannot increase nonlinearly due to the rapid fluctuations in load over a short period, while the numerical simulation assumes an ideal model for rotational speed. This is also the primary reason for the inability to accurately simulate the variation in the head during the pump startup process. Before and after the modification of the turbulence model, the same rotational speed formula was used, resulting in the same curve. With an increase in pump speed, the curvature effect becomes apparent. In the latter half of the acceleration, the improved model's trend approaches the experimental curve, demonstrating that in subsequent internal flow analysis, the improved turbulence model will exhibit better performance.

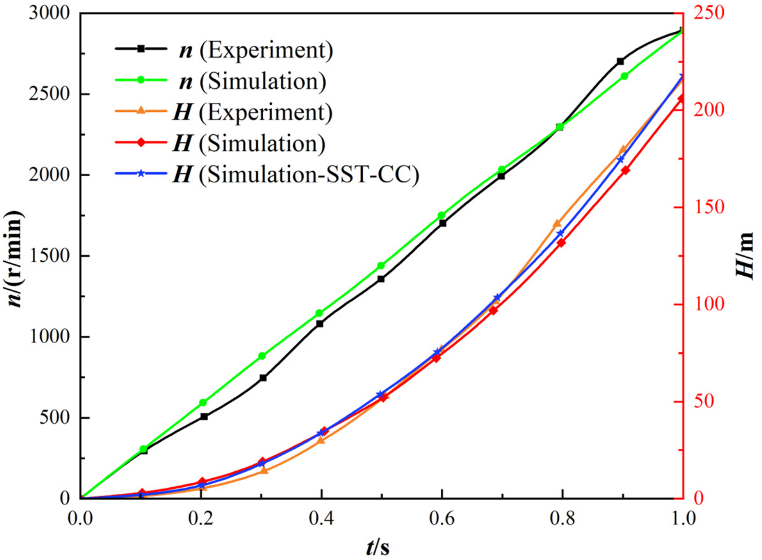

Figure 6. Comparison of simulated and experimental values of performance.

3.2. Transient Internal Flow Characteristics Analysis during the Startup Process

3.2.1. Pump Performance Analysis and Vortex Structures Evolution

Figure 7 illustrates the head variation of a multistage pump during the 1-s startup process at three different rotational speeds: 2000 r/min, 2900 r/min, and 3800 r/min. From the graph, it is evident that the trend of head variation over time is essentially the same across the different speeds. In the initial phase of the startup, although the impeller begins to rotate, the rate of head increase is low, which is related to the stationary state of the water body before startup. At the very beginning of the startup phase, due to minimal changes in the state and resistance of the water body, the head change is slow, exhibiting weak dynamic responsiveness. Along with the increase in rotational speed, the power generated by the impeller strengthens, enhancing its ability to overcome fluid resistance and causing the head to rise more rapidly, thus showing strong dynamic responsiveness. The peak head values at different rotational speeds are 97.7 m at 2000 r/min, 204.12 m at 2900 r/min, and 394.43 m at 3800 r/min. The significant differences in peak head values under different speeds indicate that the peak head variation under different operating conditions exhibits notable differences, with the dynamic characteristics depending on the operating parameters. Compared to the steady-state head under the same conditions, the peak head is 1.76%, 2.06%, and 2.99% higher at 2000 r/min, 2900 r/min, and 3800 r/min, respectively. This indicates that the head during startup experiences high amplitude fluctuations, which may have certain impacts on the system.

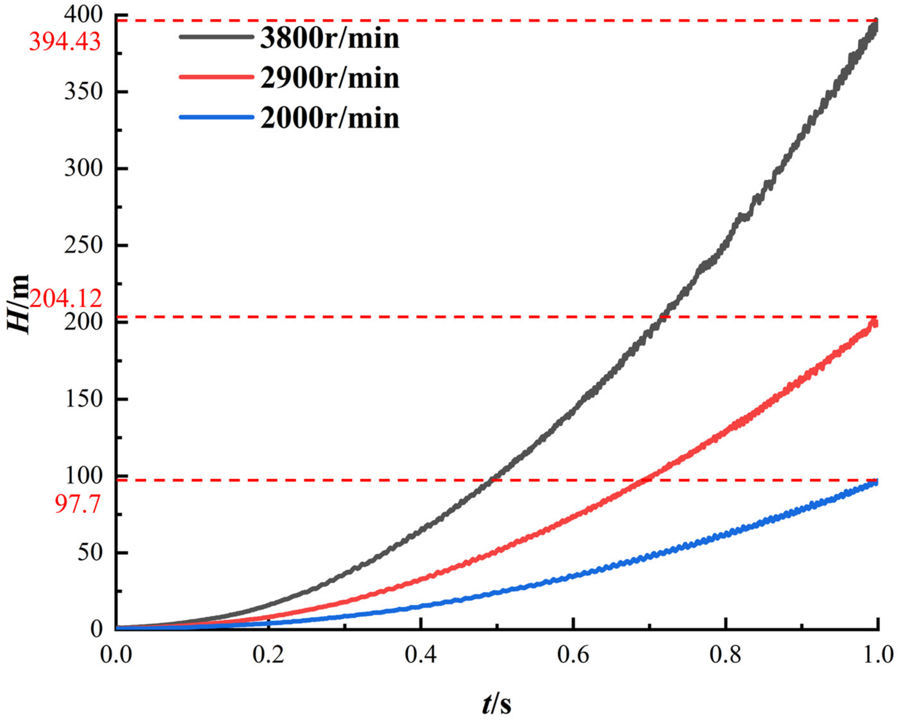

Figure 7. Startup process head variation curve.

The head variation of the multistage pump during startup is mainly dependent on the change in rotational speed. To eliminate the influence of speed and better analyze the transient characteristics of the pump during startup, the dimensionless head coefficient is used to describe the startup process. Figure 8 shows the variation of the head coefficient of the multistage pump over time during the startup process. The graph indicates that the head coefficient curves at different speeds essentially follow the same curve, demonstrating that the pump adheres to similarity laws during startup, regardless of the specific speed. The head coefficient initially decreases rapidly and then more slowly, exhibiting a maximum value at the very start of the process: 5760.36 at 2000 r/min, 3906.49 at 2900 r/min, and

3555.4 at 3800 r/min. This is related to the sudden rotation of the impeller impacting the stationary water body, reflecting the significant transient impact caused by changes in water conditions at the start of the process. The head coefficient then rapidly decreases and stabilizes at around 3.21 after 0.218 s, indicating clear transient characteristics throughout the startup process.

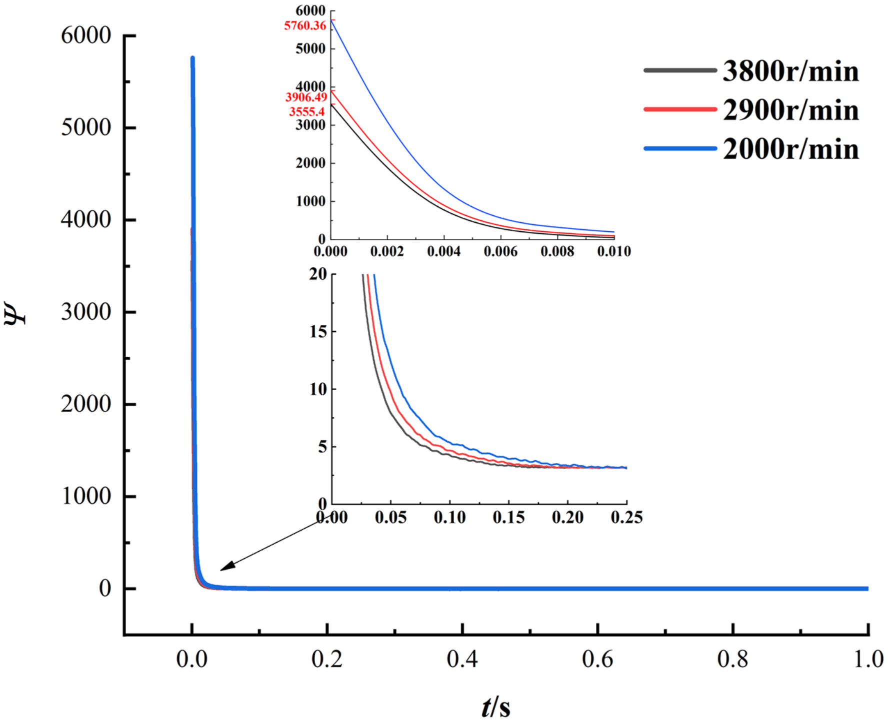

Figure 8. Startup process head coefficient variation curve.

The above analysis shows that the internal flow field of the multistage pump impeller is relatively chaotic during the startup process. The internal flow during startup is closely related to the vortices generated within the flow field. Figure 9 depicts the evolution of vortex structures within the impeller at different times during closed-valve startup. The figure shows that the vortex structures within the impeller are periodically distributed, mainly concentrated on the suction side near the inlet, the pressure side near the outlet, and within the guide vane passage. This is due to the increased pressure difference on both sides of the blade caused by the acceleration of the fluid within the impeller. Overall, the changes in vortex structures within the guide vane passage are relatively weak, with elongated vortices dominating the guide vane inlet and discontinuous band-shaped vortices at the outlet. At t = 0.3 s, the distribution of vortex structures within the impeller is sparse, mainly located near the outlet of the impeller passage, due to the lower rotational speed resulting in smaller fluid acceleration. As the speed increases, at t = 0.6 s and t = 0.9 s, the vortex structures near the outlet of the impeller passage extend upstream and develop into shedding vortices, forming elongated internal vortex clusters in the middle. This results from the increased fluid acceleration and expansion of vortex scales. At t = 1.0 s, with the rotational speed reaching its maximum, the vortex structures within the impeller passage reach their maximum development, almost covering the entire impeller passage. Overall, as the impeller speed increases, the range of vortex structures continues to expand and develop, eventually almost covering the entire impeller passage. The evolution of vortex structures reflects the increased acceleration of fluid within the impeller and the expansion of vortex scales.

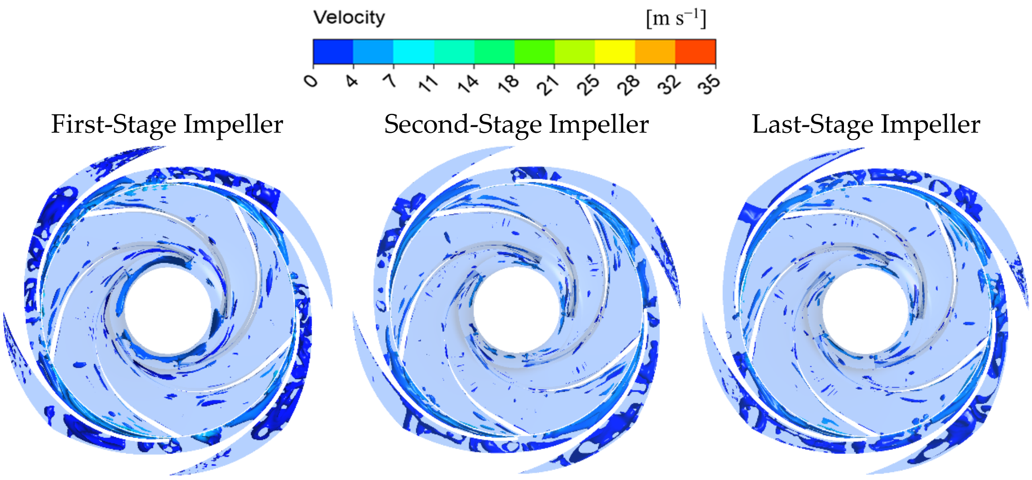

(**a**) *t* = 0.1 s

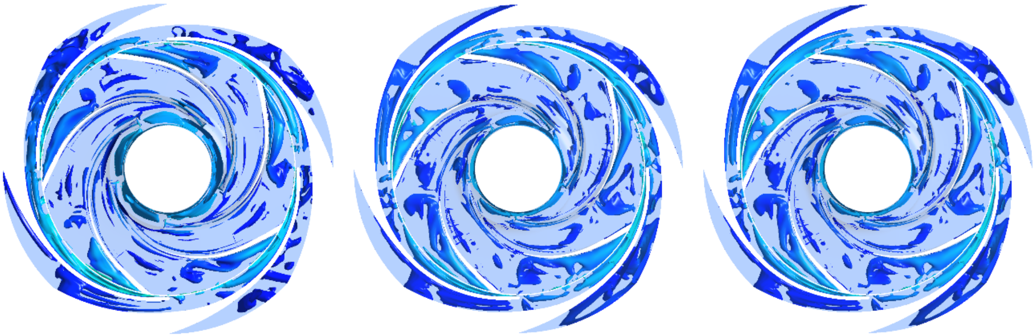

(**b**) *t* = 0.4 s

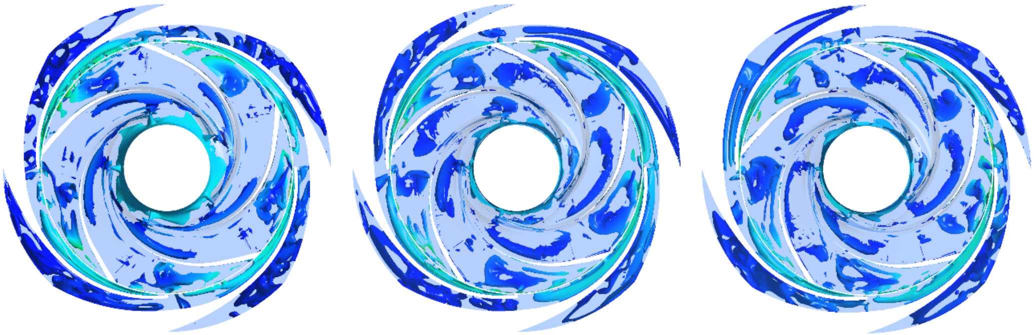

(**c**) *t* = 0.7 s

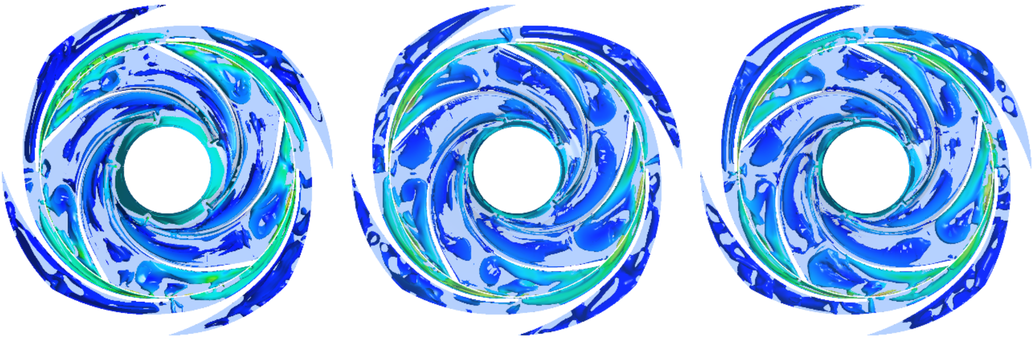

(**d**) *t* = 1.0 s

Figure 9. Startup process impeller internal vortex structure distribution.

3.2.2. Influence of Startup Time on Transient Characteristics of Multistage Pump

To better understand the degree of real-time variation in the head during the startup process of a multistage pump with different startup times, differential data statistics are performed on the head during the startup process. The head variation rate is defined as follows:

$$H_C = \frac{\Delta H}{\Delta t} \tag{18}$$

Figure 10 shows the variation of the head change rate (H_c) of the multistage pump with different startup times over time. When the startup time is in 1 s, H_c gradually increases as the startup process progresses. In the red-marked region, a brief plateau phase occurs. When the rotational speed, n, approaches the set value, H_c sharply increases to a peak and then falls back. When the startup times are 3 s and 5 s, H_c exhibits a similar trend in the early startup phase as the startup time is 1 s. In the mid-to-late startup phase, there is a more pronounced plateau period. After approaching the set rotational speed, H_c experiences a sharp increase to a peak followed by a substantial decrease.

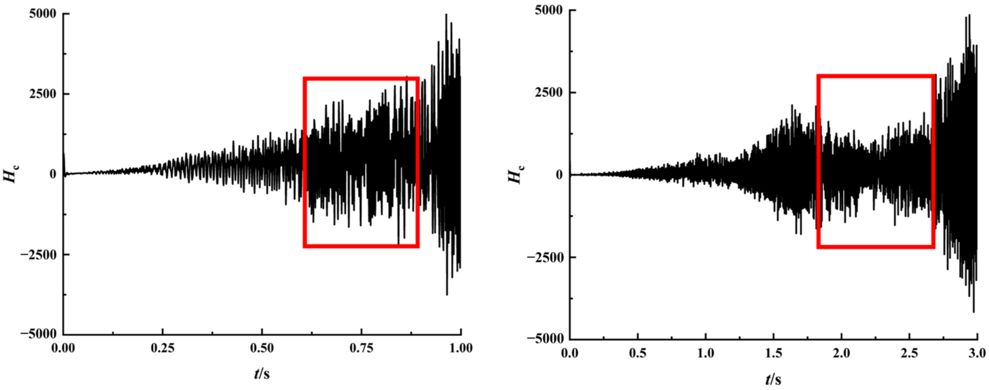

(**a**) Startup time of 1 s (**b**) Startup time of 3 s

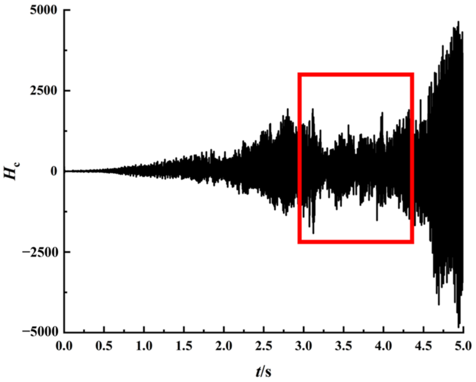

(**c**) Startup time of 5 s

Figure 10. Head change rate of the multistage pump at different startup times.

During the oscillations of H_c in its plateau phase, the head is in a relatively stable rising phase. According to the actual test results for n in Figure 6, it can be observed that the rotational speed is not linearly increasing due to the load's influence, which is in line with the characteristics of the early H_c changes as shown in Figure 10. Later, as n increases linearly, corresponding to the plateau phase of H_c, the flow inside the pump has improved compared to the early stage, with smoother velocity streamlines. Before reaching the set rotational speed, n rises faster compared to the ideal state, and at this point, the impeller passage forms two vortices, corresponding to the sharp rise and subsequent fall of H_c. In summary, when the startup time is 1 s, compared to 3 s and 5 s, the rate of head change for the multistage pump is more severe during the startup process, and the maximum rate of head change is also greater. This indicates that a shorter startup time can lead to significant differences in the rate of head change during the process, causing larger fluctuations in the operating state of the multistage pump. In contrast, a longer startup time can stabilize head changes, reducing their magnitude and contributing to the stability of the multistage pump's operation.

Figure 11 illustrates the variations and comparisons of different types of entropy production in the multistage pump under different startup times. From the graph, it can be observed that during the startup process, the trends of turbulent dissipation entropy production $S_{pro,D'}$, wall entropy production $S_{pro,W}$, and total entropy production S_{pro} are similar. They all increase with the increase in rotational speed, indicating that as the impeller speed increases, the fluid's acceleration inside the impeller intensifies, leading to an increase in various dissipative losses. The magnitude and variation of direct dissipation entropy production $S_{pro,D'}$ are relatively small compared to the other two types of entropy production. Its impact can be neglected. Turbulent dissipation entropy production $S_{pro,D'}$ is consistently greater than wall entropy production $S_{pro,W}$, and the proportion of turbulent dissipation entropy production to total entropy production exceeds 56%. This indicates that turbulent losses dominate the losses within the multistage pump, making them the primary part of the overall losses. The variation trends of entropy production under different startup times are similar. After reaching the operating speed, the total entropy production decreases with the increase in startup time. For example, the total entropy production is 70.02 W/K for a startup time of 1 s, 67.7 W/K for 3 s, and 66.94 W/K for 5 s. This indicates that with shorter startup times, the losses within the multistage pump are greater, resulting in higher total entropy production values.

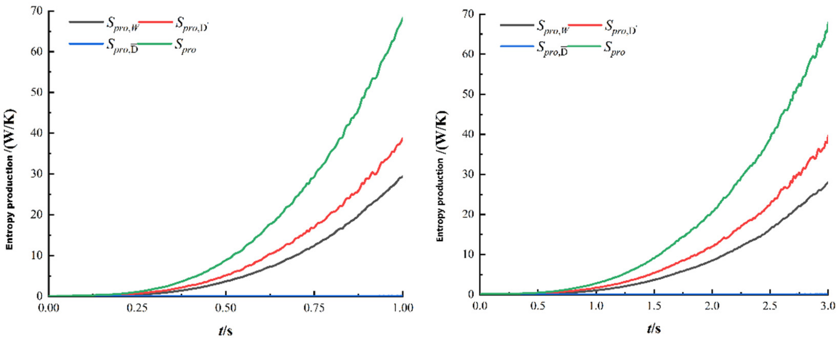

(**a**) Startup time of 1 s (**b**) Startup time of 3 s

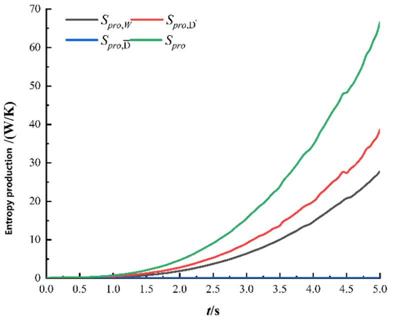

(**c**) Startup time of 5 s

Figure 11. Distribution of entropy production in the pump with different startup times.

Figure 12 shows the variations and comparisons of the total entropy production ratios for different flow components, including the suction chamber, impeller rings' gap, pump chamber, impeller, guide vanes, and volute, under different startup times. As shown in the graph, the trends of the total entropy production ratios for the various flow components are similar during the startup process. This indicates that regardless of the startup time's duration, the variation process and patterns of the entropy production ratios for each component are the same, only with different specific values. In the early stage of the startup, the guide vanes have a relatively high total entropy production ratio, followed by the pump chamber and impeller, and finally, the impeller rings, suction chamber, and volute. As the startup process progresses, the total entropy production ratio of the guide vanes and pump chamber gradually decreases, while the total entropy production ratio of other flow components increases and reaches a stable value in the later stages of startup. The total entropy production ratio of the impeller reaches a stable value earlier compared to other flow components, and it has the highest value after stabilization. This indicates that the losses during the startup process mainly occur in the impeller flow passage, followed by the pump chamber, guide vanes, impeller rings, and finally, the suction chamber and volute. For example, the total entropy production ratio of the impeller flow passage under different startup times is as follows: 42.68% for a startup time of 1 s, 41.04% for 3 s, and 40.68% for 5 s. A shorter startup time results in a larger total entropy production ratio in the impeller flow passage. This is because shorter startup times require higher acceleration of the impeller, which intensifies the slip between the fluid and the impeller, resulting in more energy losses in a short period. Such energy losses result in rapid vortex evolution, leading to the formation of pressure fluctuations that impact the pump's stable operation.

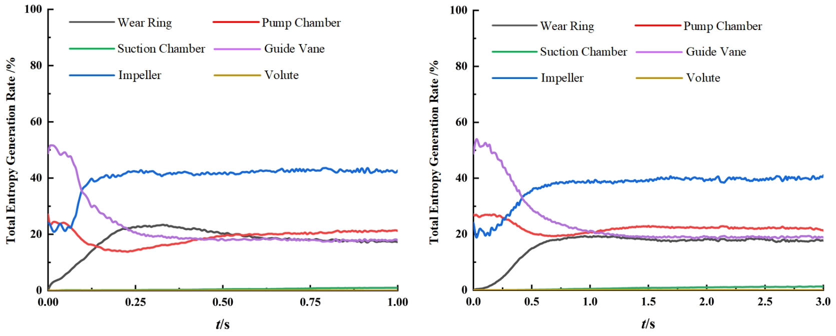

(**a**) Startup time of 1 s (**b**) Startup time of 3 s

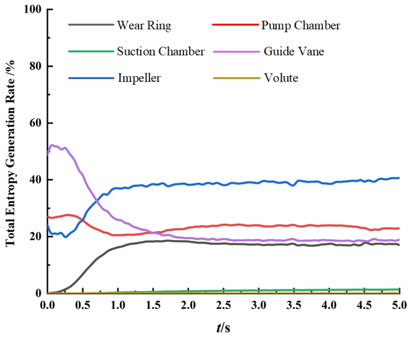

(**c**) Startup time of 5 s

Figure 12. Variation of total entropy production ratio of overcurrent components at different startup times.

3.2.3. Time–Frequency Analysis of the Pressure Pulsation

The pressure pulsation time-domain characteristics of the multistage pump during the startup process are shown in Figure 13. From the graph, it can be observed that different stages of the multistage pump exhibit significant variations in pressure pulsation time-domain characteristics. At the initial startup, the pressure values (C_p) at various monitoring points in the first stage show significant differences, while those in the subsequent stages are relatively concentrated, especially in the last stage. This clearly illustrates the dynamic characteristics of each stage of the multistage pump at the moment of startup. Furthermore, at point A1, located at the inlet of the first-stage impeller, there is minimal fluctuation in C_p due to the startup with the ball valve fully closed, indicating a relatively stable state of static fluid. Monitoring points A2 to A6, as well as those in the subsequent and last stages, all show an increasing trend in pressure pulsation coefficient with the acceleration of the impeller. Monitoring points A2 and A3 in the first stage display a widening fluctuation range of the pressure pulsation coefficient with increasing impeller speed, while monitoring points A4 to A6 at the guide vanes show a slight increase in the pressure pulsation coefficient. The fluctuation range at monitoring points B1 to B3 in the subsequent stage is also significant, with B1 showing a periodic acceleration pattern and B2 and B3 exhibiting a similar pattern as the previous stage but with reduced intensity. In the last stage, the trajectories of all monitoring points are relatively consistent, with C3 showing an intensified fluctuation towards the end of the startup process. The significant amplitude of pressure pulsation at monitoring points A3, B3, and C3 near the impeller's flow outlet is due to the structural arrangement of each stage of the multistage pump, resulting in more drastic pressure changes near the impeller's flow outlet. As mentioned in the previous analysis of entropy production, it can be inferred that the impeller with the highest entropy production dominates the end stage of the startup phase.

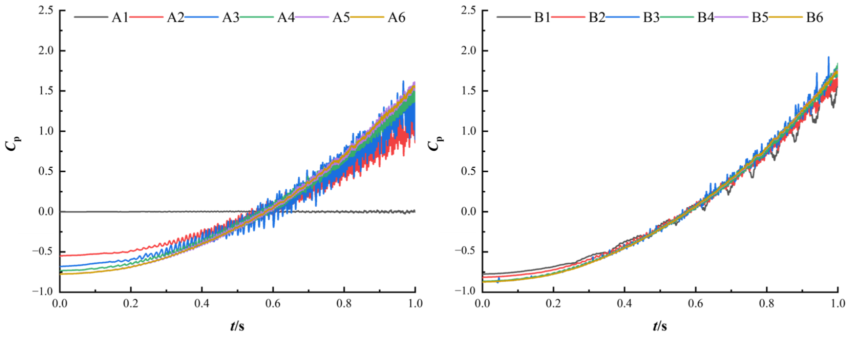

(**a**) First-stage impeller (**b**) Second-stage impeller

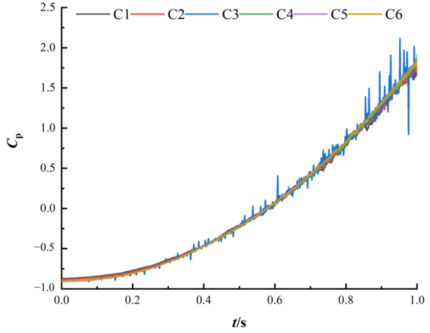

(**c**) Last-stage impeller

Figure 13. Pressure pulsation time-domain characteristics.

The pressure pulsation characteristics during the startup process of the multistage pump exhibit not only time-domain features but also prominent frequency-domain features. However, the frequency-domain signal analysis, primarily based on the Fourier Transform, mainly focuses on frequency information while completely disregarding time information, thus being unable to represent the frequency spectrum distribution of a signal at a particular moment. To explore the pressure pulsation characteristics during the startup process more accurately, this study employs wavelet transform to analyze the pressure data obtained from transient calculations [29]. The pump is designed to operate at a rotational speed of 3800 rpm, corresponding to a rotational frequency, i.e., shaft frequency, of 63.33 Hz.

Due to significant differences in C_p values among various monitoring points in the first stage, further analysis is required. Figure 14 illustrates the time–frequency domain characteristics of pressure pulsation at different monitoring points of the first stage of the multistage pump during the startup process. The plot is generated based on the startup time and frequency, with different colors representing the magnitude of frequency amplitudes. The figure shows that as the rotational speed increases, the overall frequency of pressure pulsation tends to increase, and the amplitude of pressure pulsation gradually amplifies. In different monitoring points within the impeller flow passage, the time–frequency plots exhibit multiple dominant frequency components, with the dominant component related to the number of blades in the guide vanes and corresponding to four times the rotational frequency. Other components appear at the harmonics of the rotational frequency. From the A1 monitoring point to the A3 monitoring point, the amplitude of pressure pulsation frequency components gradually increases. Moreover, in the time–frequency plot of the A3 monitoring point, multiple discontinuous frequency components with different amplitudes can be observed, indicating that the fluctuations within the impeller flow passage become more intense along the flow direction. In the guide vane flow passage, the time–frequency plots also exhibit multiple dominant frequency components, with the dominant component corresponding to five times the rotational frequency, which is the passing frequency of the impeller flow passage blades. From the A4 monitoring point to the A6 monitoring point, the amplitude of pressure pulsation frequency components gradually decreases, indicating that the fluctuations within the guide vane flow passage become smoother along the flow direction. Furthermore, except for point A1, the time–frequency plots of all monitoring points show a phenomenon of concentrated pressure pulsation amplitude, continuously existing in the low-frequency range below one time the shaft frequency. Additionally, within the low-frequency range, the amplitude tends to increase with the acceleration of the impeller, indicating the presence of strong low-frequency pulsation within the pump.

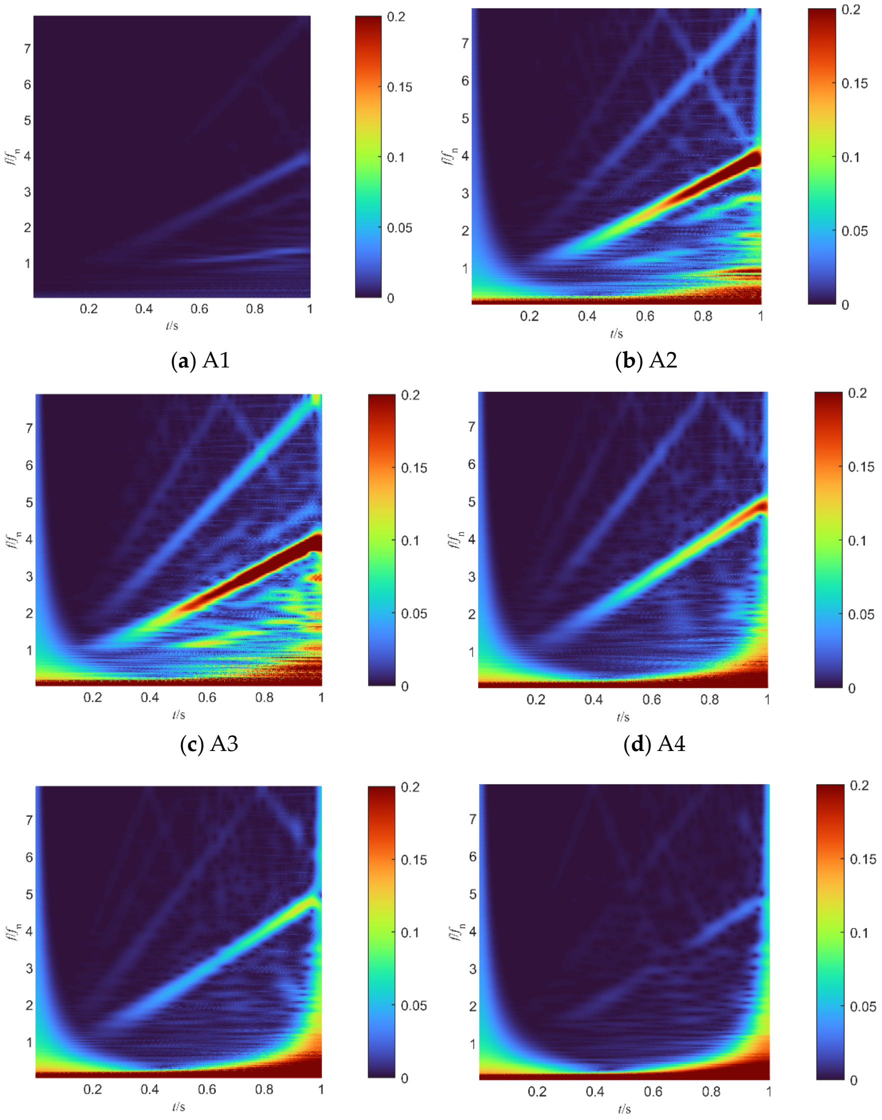

(**a**) A1 (**b**) A2

(**c**) A3 (**d**) A4

(**e**) A5 (**f**) A6

Figure 14. Pressure pulsation time–frequency domain characteristics during the startup process.

3.3. Transient Internal Flow Characteristics Analysis during the Valve Opening Process

3.3.1. Pump Performance Analysis and Vortex Structures Evolution

Figure 15 shows the external characteristic curves under different flow variation patterns during the valve opening process. From the figure, it is evident that the entire valve opening process exhibits significant transient response characteristics. In the initial stage of valve opening, the flow rate changes suddenly, resulting in a significant transient in the external characteristics, with a noticeable drop in the head. As the flow rate gradually increases, the head starts to rise and then gradually decreases after the flow rate reaches around 21.6 m^3/h, stabilizing at approximately 345.79 m. Under different flow variation patterns, the degree of head change varies. The head trough for the exponential flow variation pattern is 320.19 m, significantly lower than the 329.01 m for the linear flow variation pattern, indicating that the head drop amplitude is smaller under the linear flow variation pattern, with a higher head trough value. The efficiency of the multistage pump increases rapidly initially and then more gradually with increasing flow rate. Although the final efficiency values are similar under different flow variation patterns, the exponential flow variation pattern achieves a higher efficiency more quickly.

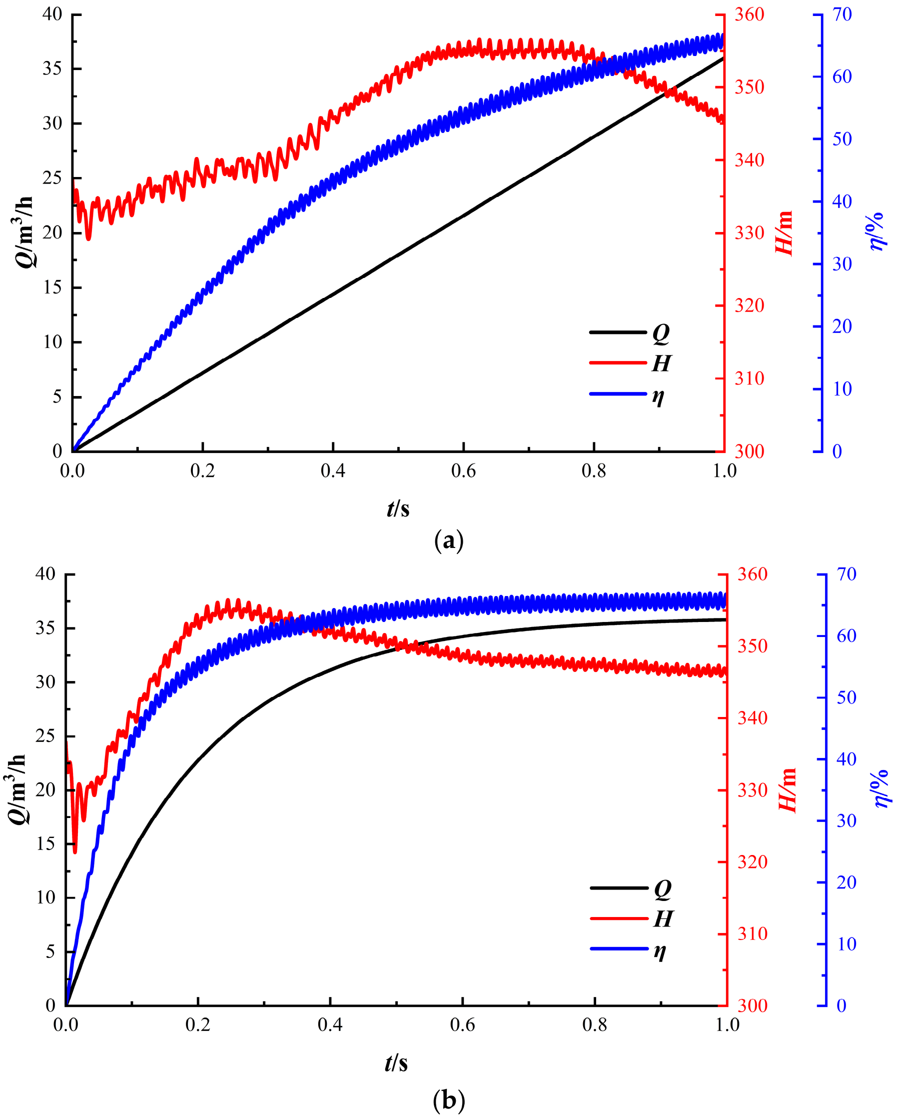

(**a**)

(**b**)

Figure 15. Open-valve process external characteristic change curve: (**a**) linear flow variation and (**b**) exponential flow variation.

Figure 16 illustrates the head rate of change under different flow variation patterns during the valve opening process. From the figure, it can be seen that different flow variation patterns (linear and exponential) lead to different head rates of change patterns. Linear flow variation causes significant fluctuations in the head rate of change, especially in the early stage of valve opening, whereas exponential flow variation results in a large peak in the head rate of change, which then stabilizes quickly. The rapid initial increase in flow rate under the exponential flow variation pattern causes a sharp change in the head, leading to dramatic fluctuations in the head rate of change. However, as the flow rate change slows down, the fluctuations in the head rate of change become relatively stable. In the later stages of valve opening, the exponential flow variation still causes slight fluctuations in the head rate of change within a lower range, but the overall change trend remains a steady decline.

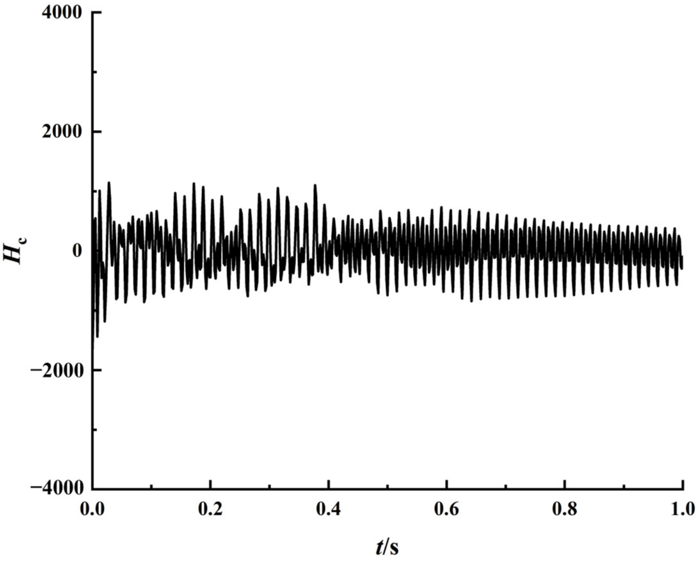

(**a**)

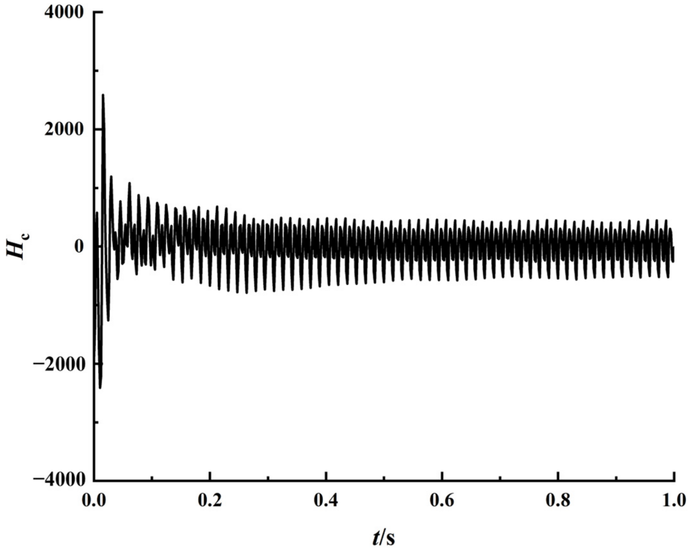

(**b**)

Figure 16. Head change rate for different flow rate variation patterns: (**a**) linear flow variation and (**b**) exponential flow variation.

Figure 17 compares the transient flow–head curves with the steady-state test flow–head curves under different flow variation patterns. From the figure, it can be seen that the transient curves are generally below the steady-state curves, except for the head surge at the initial stage of valve opening. The transient and steady-state curves exhibit similar trends with flow rate changes. As the flow rate increases, the fluid velocity increases, with part of the energy used to accelerate the fluid, resulting in a lower head during the valve opening process. When the flow rate approaches the design operating point, the phenomenon of separation and reattachment in the impeller decreases, causing the transient curves to gradually approach the steady-state curves. The range of head change for the exponential flow variation pattern is larger than that for the linear flow variation pattern, which is related to the higher initial flow rate increase for the exponential flow variation pattern. Besides the head surge, the flow–head curves under different flow variation patterns show good consistency.

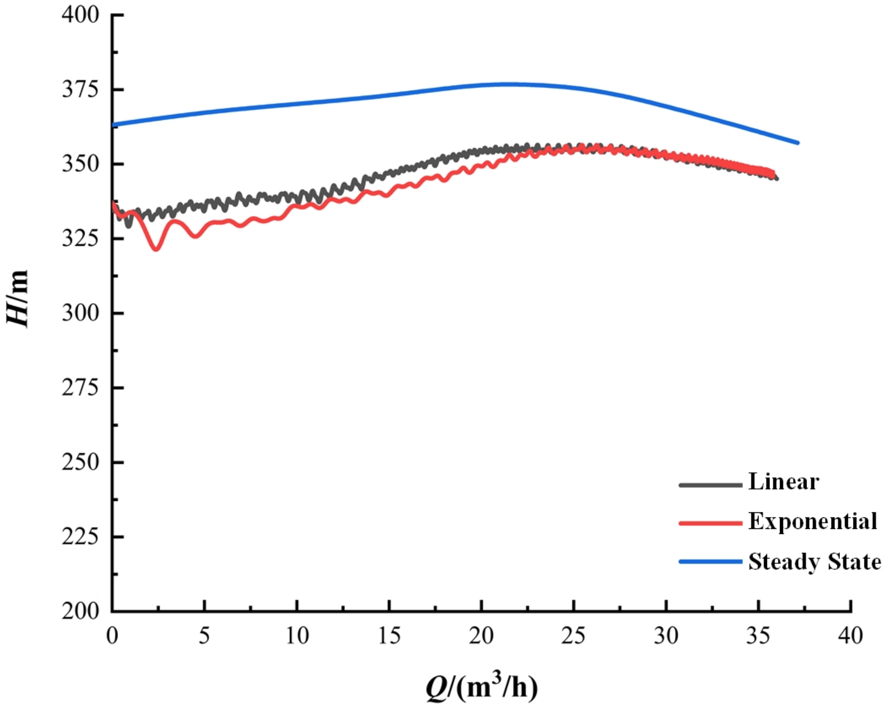

Figure 17. Comparison of transient and steady test curves.

The vortex structure within a multistage pump is closely related to the velocity, and the vortex structure is highly sensitive to changes in velocity. When operating conditions change, the stability of the vortex structure may be affected. Therefore, based on vortex identification methods, the changes in the impeller vortex structure at two different moments under varying flow rates of a multistage pump are selected to study the changes in the impeller vortex structure during the valve opening process. These two moments are t = 0.4 s, when the internal pump velocity shows significant differences under different flow rate variations, and t = 1.0 s, when the internal pump velocity shows minimal differences under different flow rate variations, as shown in Figure 18.

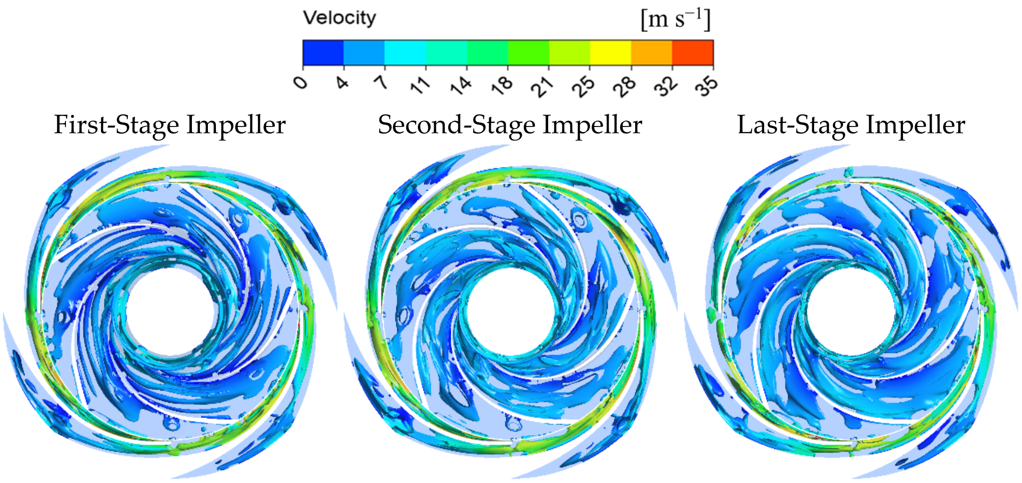

(**a**) Linear flow variation at *t* = 0.4 s

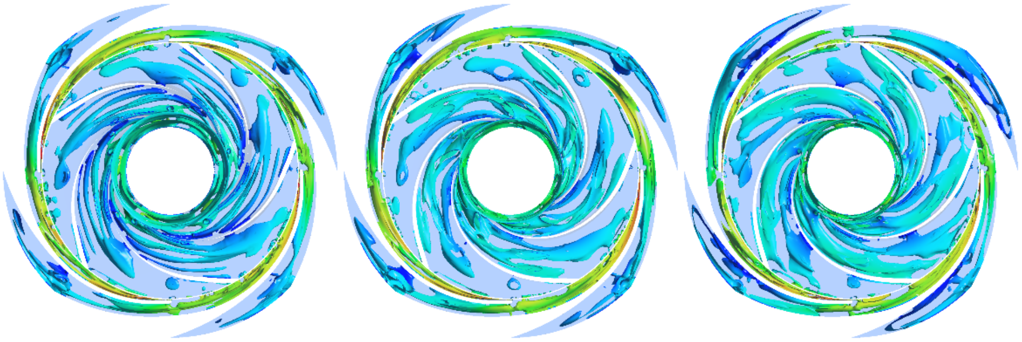

(**b**) Exponential flow variation at *t* = 0.4 s

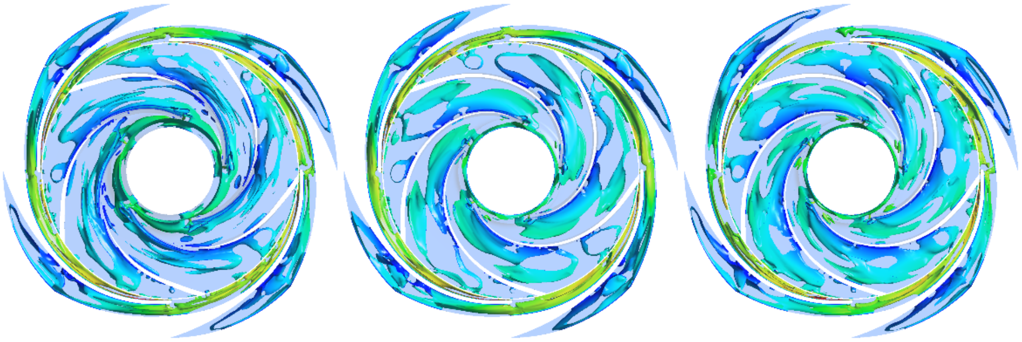

(**c**) Linear flow variation at *t* = 1.0 s

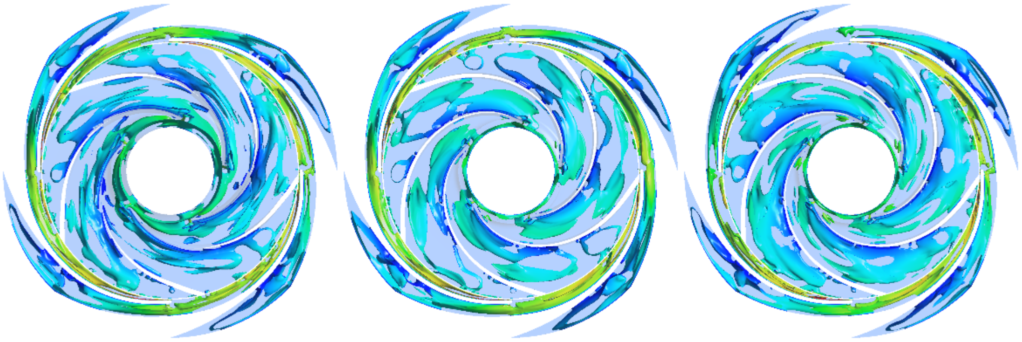

(**d**) Exponential flow variation at *t* = 1.0 s

Figure 18. Open-valve process of impeller internal vortex structure distribution.

From Figure 18, it can be observed that at *t* = 0.4 s, the vortex structure distribution within each stage impeller under the linear flow variation pattern is relatively similar, mainly characterized by an inner rotating passage vortex occupying almost the entire impeller channel. The shape of the vortex structure shows slight differences across different stage impellers: in the first-stage impeller, the passage vortex is elongated near the impeller channel inlet, while in the subsequent two-stage impellers, the vortex shape is more irregular. This indicates that the shape of the vortex structure is influenced by flow conditions and geometric factors, resulting in differences across different stage impellers. Compared to the linear flow variation pattern, the vortex structure distribution range within the impeller channels is significantly reduced under the exponential flow variation pattern due to the larger flow rate. At t = 1.0 s, the flow rate reaches the design flow rate, causing the vortex structure to further break up, leading to a reduced vortex structure range. The vortex structure distribution exhibits similarity under both linear and exponential flow variation patterns, indicating that at the design flow rate, the vortex structure distribution tends to be similar regardless of the flow variation pattern. Additionally, with the increase in the number of stages, the energy conversion of the fluid in the channels becomes more sufficient, resulting in an enlarged vortex structure range accordingly.

3.3.2. Entropy Production Diagnosis

Figure 19 illustrates the variation in the total entropy generation rate for different flow components under varying flow rate conditions during the valve opening process. From the figure, it can be observed that under linear flow rate variation, the total entropy generation rate of different flow components changes continuously with the flow rate. Specifically, the total entropy generation rate of the impeller passages decreases with the increase in flow rate, reducing from 42.12% to 16.28%. Conversely, the total entropy generation rates of the guide vanes and pump chamber increase with the flow rate, rising from 22.23% and 18.46% to 37.25% and 29.02%, respectively. Meanwhile, the total entropy generation rates for the wear ring, suction chamber, and volute exhibit relatively minor changes compared to other flow components. Under exponential flow rate variation, the changes in total entropy generation rates of various flow components are similar to those under linear flow rate variation in the early stages of valve opening, but they reach stable values earlier. The stable values of total entropy generation rates for each flow component are only slightly different from those at the end of the valve opening under linear flow rate variation.

Figures 20 and 21 analyze the local entropy generation rates and wall entropy generation rates distribution for the impeller and guide vanes during the valve opening process. From Figure 20, at t = 0.1 s, the local entropy generation rates are mainly distributed near the inlet of the impeller passages and near the outlet of the impeller passages and the inlet of the guide vane passages. The local entropy generation rate near the inlet of the impeller passages is relatively low, whereas the distribution near the outlet of the impeller passages and the inlet of the guide vane passages is broader, and the values are relatively higher. At t = 1.0 s, the distribution range and values of local entropy generation rates in the impeller and guide vanes decrease, and the high local entropy generation rate region near the outlet of the impeller passages disappears. This is because, at the initial stage of flow increase, the fluid cannot be adequately accelerated in the passages near the impeller outlet, leading to significant backflow and vortices. As the flow rate continues to increase, the pressure difference inside the pump rises, the average flow velocity within the pump increases, and the phenomena of flow separation and turbulence weaken, reducing the local entropy generation rates in the impeller and guide vanes. From Figure 21, at t = 0.1 s, the wall entropy generation rate distribution is similar to the local entropy generation rate distribution at the same moment, primarily located near the inlet of the impeller passages and near the outlet of the impeller passages and the inlet of the guide vane passages. At t = 1.0 s, the distribution range and values of wall entropy generation rates in the impeller and guide vanes increase. In addition to the areas near the inlet of the impeller passages and near the outlet of the impeller passages and the inlet of the guide vane passages, a relatively extensive but lower-value wall entropy generation area forms in the middle of the impeller passages. This is due to the increase in flow rate, which enhances the velocity gradient within the boundary layer and increases viscous resistance and frictional losses, thereby enlarging the distribution range and values of wall entropy generation rates in the impeller and guide vanes.

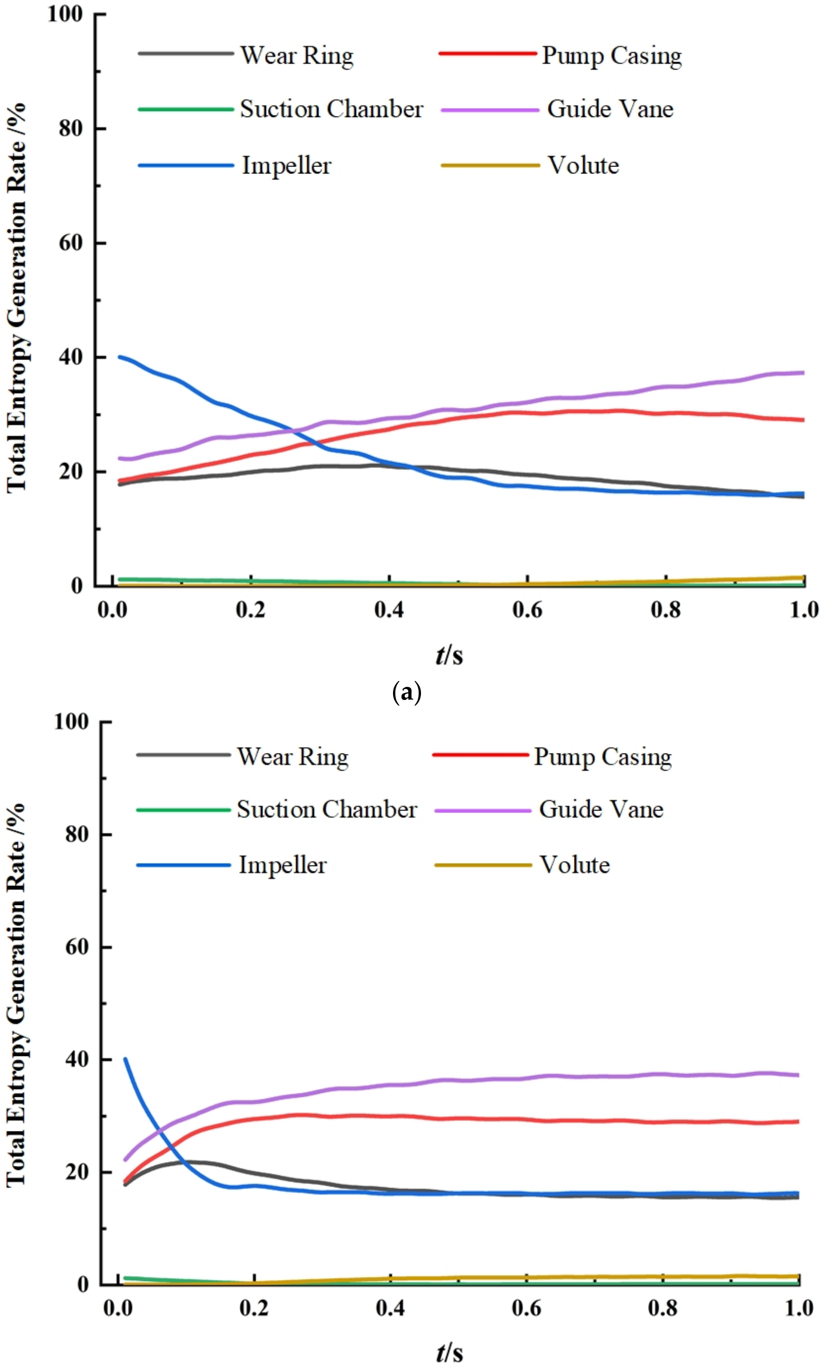

(**a**)

(**b**)

Figure 19. Open-valve process of the total entropy production ratio variation of overcurrent components: (**a**) linear flow variation and (**b**) exponential flow variation.

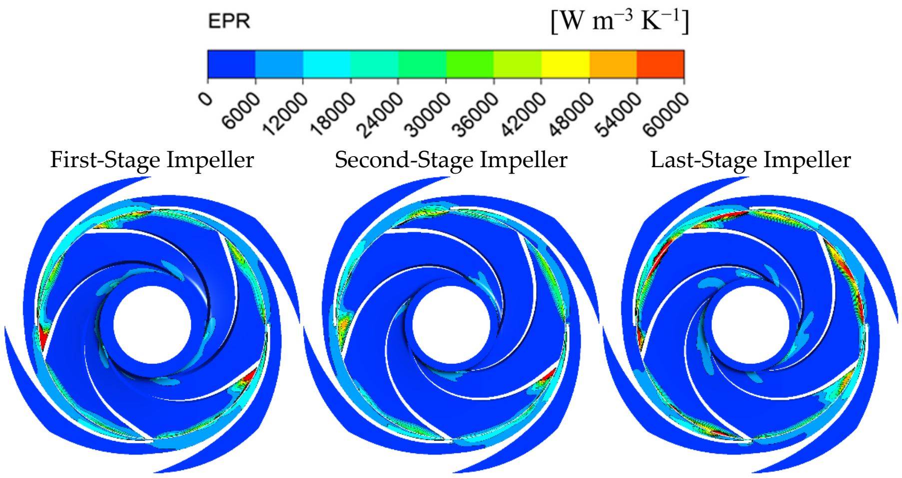

(**a**) At t = 0.1 s

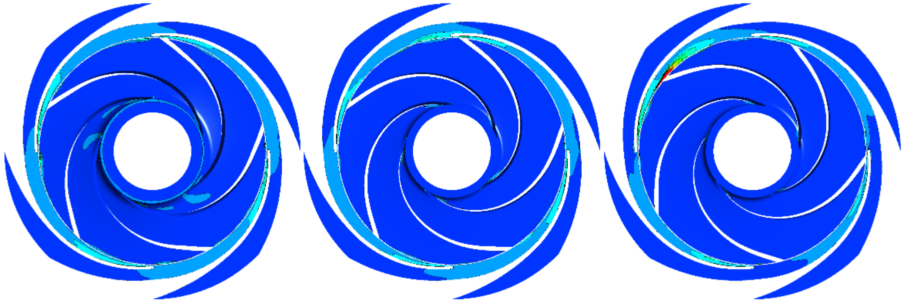

(**b**) At t = 1.0 s

Figure 20. Open-valve process of the local entropy production rate variation.

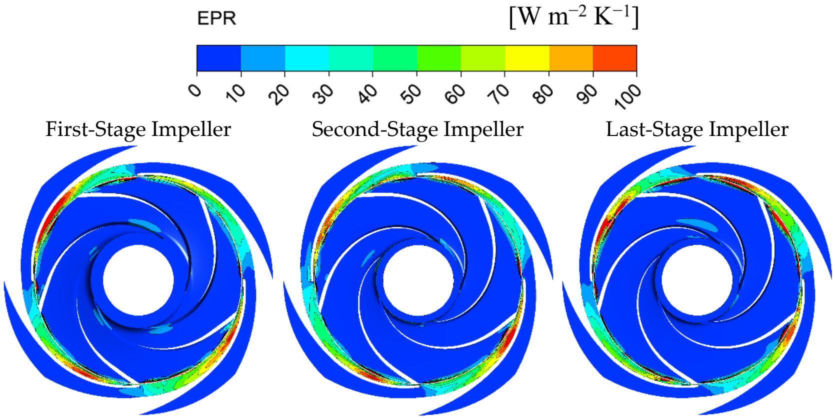

(**a**) At t = 0.1 s

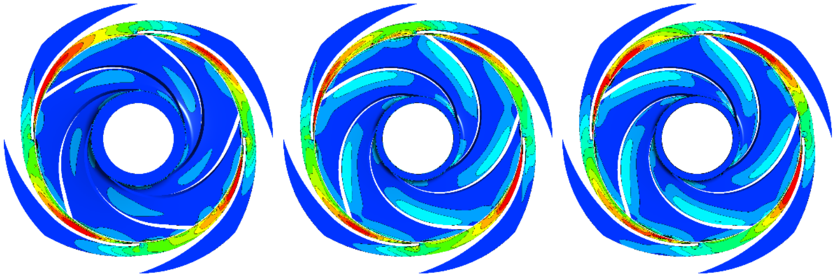

(**b**) At t = 1.0 s

Figure 21. Open-valve process of the wall entropy production rate variation.

Based on Figures 19–21, it can be seen that during the valve opening process, the local entropy generation rate in the impeller and guide vane flow channels gradually decreases with the increase in flow rate, while the wall entropy generation rate increases with the increase in flow rate. Due to the different magnitudes of variation of local entropy generation and wall entropy generation within the impeller and guide vane flow channels, the combined effect of both causes the total entropy generation rate in the impeller flow channel to decrease while the total entropy generation rate in the guide vane flow channel increases during the valve opening process.

3.3.3. Time–Frequency Analysis of the Pressure Pulsation

Figure 22 shows the time–frequency domain characteristics of pressure pulsation at various monitoring points of the first stage of a multistage pump during the valve opening process. From the figure, it can be seen that the pressure pulsation frequency remains almost constant with changes in flow rate during the valve opening process, while the amplitude of pressure pulsation decreases with the increase in flow rate. In the time–frequency diagram of the impeller flow channel, there are multiple frequency components with dominant amplitudes, with the main component related to the number of guide vane blades, corresponding to four times the rotational frequency, and other components appearing at multiples of the rotational frequency. At monitoring point A1, a concentration of pressure pulsation amplitude is observed, continuously existing in the low-frequency range below twice the shaft frequency, with a decreasing trend in the low-frequency range as the flow rate increases. At monitoring point A3, besides the four times rotational frequency, there are several frequency components with discontinuous amplitudes. In the guide vane flow channel, the time–frequency diagram shows multiple frequency components with dominant amplitudes, with the main component corresponding to five times the rotational frequency, which is the blade passing frequency of the impeller flow channel, and other components appearing at multiples of the rotational frequency. The amplitude of the main frequency component at monitoring points A4 to A6 changes little over time, and there is a decreasing trend in the amplitude of the main frequency component along the flow direction from A4 to A6.

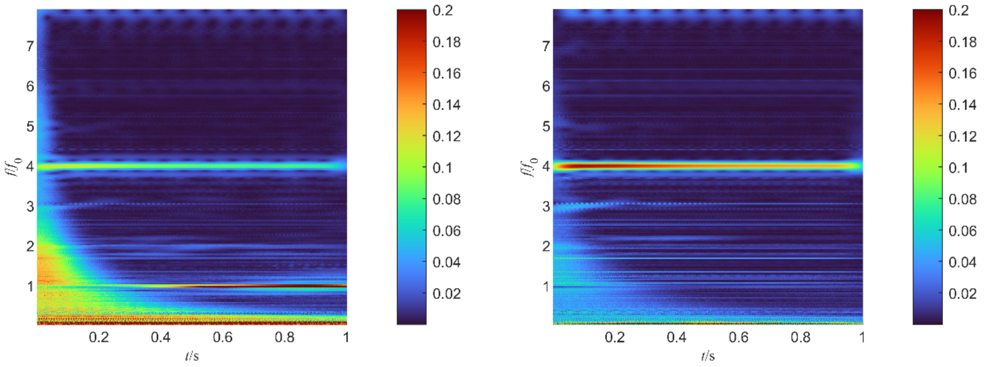

(**a**) A1 (**b**) A2

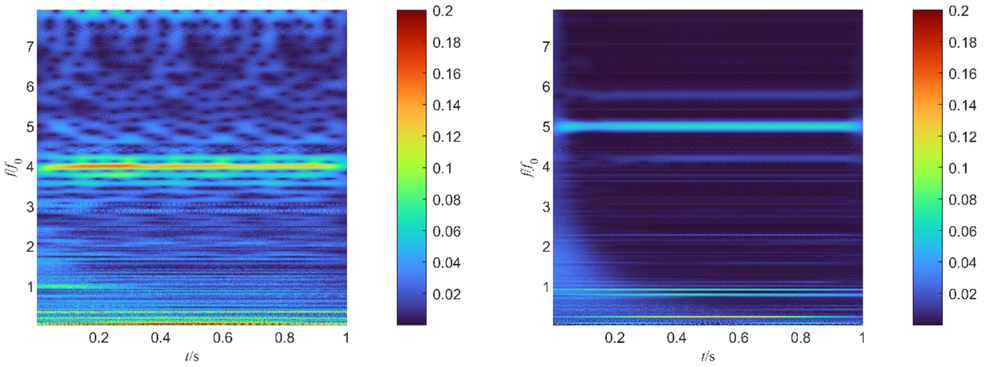

(**c**) A3 (**d**) A4

Figure 22. *Cont.*

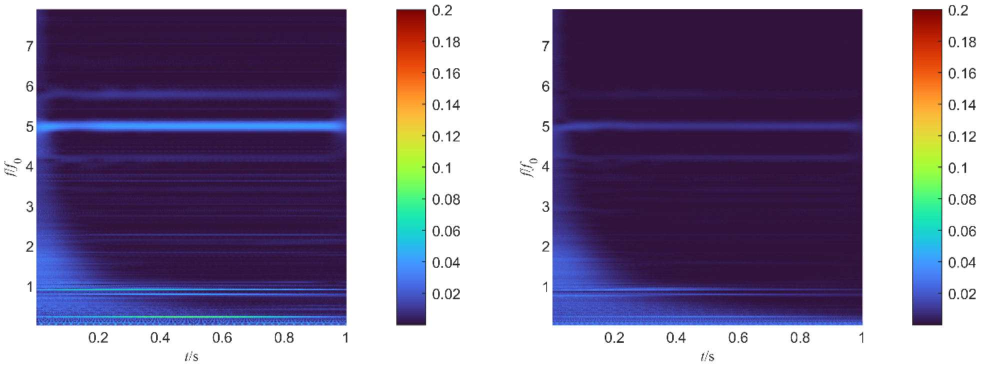

(**e**) A5 (**f**) A6

Figure 22. Pressure pulsation time–frequency domain characteristics during the Valve Opening Process.

4. Conclusions

This paper adopts a method of controlling the variation of impeller speed in multistage pumps. It conducts numerical simulations of the startup process of emergency water supply multistage pumps with the valve fully closed. From various perspectives, such as performance, vortex structures, entropy generation, and pressure pulsation, the changing characteristics of important performance parameters during the startup process are revealed. The internal flow characteristics are compared and analyzed under different startup times. The main research findings are as follows.

When the startup time of a multistage pump is 1 s, the head variation trend over time is consistent across different operating speeds. As the rotational speed increases, the head change initially shows a slow trend followed by a rapid increase, reaching a peak after attaining maximum speed. Simultaneously, the vortex structure range expands and develops with the increase in impeller speed, covering a larger area. At a 1-s startup time, the vortex structure within the impeller passage reaches its maximum development state, almost covering the entire impeller passage. The evolution of the vortex structure reflects the increase in fluid acceleration and the expansion of the vortex scale within the impeller. Moreover, as the impeller speed increases, the frequency and amplitude of pressure pulsations also increase, showing the same trend as speed variations.

Under different startup times, the head variation curves of the multistage pump exhibit similar patterns. As the impeller speed increases, the head shows an initial slow rise followed by a rapid increase, reaching a peak at the end of impeller acceleration. However, with shorter startup times, the transient effects of the pump are stronger, leading to more severe head variations and higher peak head values. Additionally, under different startup times, the entropy generation trends are similar. After reaching operating speed, the total entropy generation decreases with increasing startup time; shorter startup times result in higher losses within the multistage pump, leading to higher total entropy generation. The total entropy generation ratio of flow components shows similar trends, with the impeller′s total entropy generation ratio stabilizing earlier than other flow components and remaining the highest once stable, indicating that losses mainly occur in the impeller passage during startup.

During the initial stage of valve opening, the flow rate changes suddenly, causing significant transient changes in external characteristics, with a noticeable drop in the head. As the flow rate gradually increases, the head starts to rise. Under an exponential flow rate change pattern, the head drop is more significant, resulting in a lower trough head value of 320.19 m and achieving higher efficiency more quickly. The transient performance curves during the valve opening process are clearly below the steady-state performance curves. Both transient and steady-state curves exhibit similar trends with flow rate, gradually converging as the flow rate increases. Under different flow rate change patterns, the exponential flow rate change results in a faster increase in flow rate, significantly reducing the distribution range of the vortex structure within the impeller passage, enabling quicker stabilization of the flow.

During the valve opening process, as the flow rate increases, the local entropy generation rate within the impeller and guide vane passages gradually decreases, while the wall entropy generation rate increases with the flow rate. Due to the different magnitudes of changes in local and wall entropy generation rates within the impeller and guide vane passages, the combined effect leads to a decrease in the total entropy generation ratio within the impeller passage and an increase in the guide vane passage during the valve opening process. As the flow rate changes, the dominant frequency of pressure pulsation amplitude remains basically unchanged, while the pressure pulsation amplitude decreases with the increase in flow rate.

Author Contributions: C.C.: conceptualization, methodology, writing—original draft. H.X.: writing—review and editing. F.D.: writing—review and editing. K.W.: data curation, validation. Z.Z.: conceptualization, validation. Q.S.: writing—review and editing, supervision. All authors have read and agreed to the published version of the manuscript.

Funding: This research was funded by the National Key Research and Development Program of China (Grant No. 2022YFC3204603, 2023YFD1900703), the Key Research and Development Program of Jiangsu Province (BE2021379), and the engineering projects for significant scientific and technological achievements of Wuhu City (2022zc07).

Data Availability Statement: The data that have been used are confidential.

Conflicts of Interest: Author Zhen Zhang is employed by the company Jiangsu Branch of China Academy of Machinery Science and Technology Group Co., Ltd. The remaining authors declare that the research was conducted in the absence of any commercial or financial relationships that could be construed as a potential conflict of interest.

Nomenclature

H	Head (m)
n	Rotational speed (r/min)
C_p	Pressure fluctuation coefficient
H_c	Head variation rate
n_f	Operational rotational speed (r/min)
t	Current time (s)
T	Total time (s)
ψ	Head coefficient $\psi = \frac{gH}{u_2^2}$
u_2	The circumferential velocity (m/s)
P	The instantaneous pressure (Pa)
ρ	Density (kg/m^3)
$S_{pro,\overline{D}}$	Direct dissipation entropy production (W/K)
$S_{pro,D'}$	Turbulent dissipation entropy production (W/K)
$S_{pro,W}$	Wall entropy production (W/K)
S_{pro}	Total entropy production (W/K)
f_0	Shaft frequency (Hz)
Q	Flow rate (m^3/h)
η	Efficiency (%)

Abbreviations

SST	Shear stress transport
GGI	General grid interface
VFD	Variable frequency drive
Y+	Dimensionless wall distance
SWMM	Storm water management model
PSO	Particle swarm optimization
CFD	Computational fluid dynamics

References

1. Wang, C.; He, X.; Shi, W.; Wang, X.; Wang, X.; Qiu, N. Numerical study on pressure fluctuation of a multistage centrifugal pump based on whole flow field. *AIP Adv.* **2019**, *9*, 035118. [CrossRef]
2. Luna, T.; Ribau, J.; Figueiredo, D.; Alves, R. Improving energy efficiency in water supply systems with pump scheduling optimization. *J. Clean. Prod.* **2019**, *213*, 342–356. [CrossRef]
3. Zhang, Y.L.; Zhu, Z.C.; Zhao, Y.J.; Wu, J.; Zhou, F.L. Comparative experiments on a self-priming pump delivering water medium during rapid and slow starting periods. *Iran. J. Sci. Technol. Trans. Mech. Eng.* **2021**, *45*, 1007–1019. [CrossRef]
4. Li, Z.; Wu, D.; Wang, L.; Huang, B. Numerical simulation of the transient flow in a centrifugal pump during starting period. *ASME J. Fluids Eng.* **2010**, *132*, 081102. [CrossRef]
5. Wang, H.; Lei, X.; Khu, S.-T.; Song, L. Optimization of pump start-up depth in drainage pumping station based on SWMM and PSO. *Water* **2019**, *11*, 1002. [CrossRef]
6. Liu, M.; Han, Y.; Tan, L.; Lu, Y.; Ma, C.; Gou, J. Theoretical prediction model of transient performance for a mixed flow pump under fast start-up conditions. *Phys. Fluids* **2023**, *35*, 025125. [CrossRef]
7. Li, W.; Huang, Y.; Ji, L.; Ma, L.; Agarwal, R.K.; Awais, M. Prediction model for energy conversion characteristics during transient processes in a mixed-flow pump. *Energy* **2023**, *271*, 127082. [CrossRef]
8. Kan, K.; Zheng, Y.; Chen, H.; Cheng, J.; Gao, J.; Yang, C. Study into the improvement of dynamic stress characteristics and prototype test of an impeller blade of an axial-flow pump based on bidirectional fluid–structure interaction. *Appl. Sci.* **2019**, *9*, 3601. [CrossRef]
9. Ren, Z.; Sun, M.; Zhang, J.; Wang, X.; Huang, Z.; Xu, J.; Huang, C. Start-up strategy of mixed-flow pump system with impulse operation. *Ocean Eng.* **2023**, *277*, 114058. [CrossRef]
10. Fu, S.; Zheng, Y.; Kan, K.; Chen, H.; Han, X.; Liang, X.; Liu, H.; Tian, X. Numerical simulation and experimental study of transient characteristics in an axial flow pump during start-up. *Renew. Energy* **2020**, *146*, 1879–1887. [CrossRef]
11. Kan, K.; Xu, Z.; Chen, H.; Xu, H.; Zheng, Y.; Zhou, D.; Muhirwa, A.; Maxime, B. Energy loss mechanisms of transition from pump mode to turbine mode of an axial-flow pump under bidirectional conditions. *Energy* **2022**, *257*, 124630. [CrossRef]
12. Yang, Z.; Cheng, Y.; Xia, L.; Meng, W.; Liu, K.; Zhang, X. Evolutions of flow patterns and pressure fluctuations in a prototype pump-turbine during the runaway transient process after pump-trip. *Renew. Energy* **2020**, *152*, 1149–1159. [CrossRef]
13. Yun, L.; Bin, L.; Jie, F.; Rongsheng, Z.; Qiang, F. Research on the transient hydraulic characteristics of multistage centrifugal pump during start-up process. *Front. Energy Res.* **2020**, *8*, 76. [CrossRef]
14. Lu, Y.; Tan, L.; Han, Y.; Liu, M. Cavitation-vibration correlation of a mixed flow pump under steady state and fast start-up conditions by experiment. *Ocean Eng.* **2022**, *251*, 111158. [CrossRef]
15. Zhu, G.; Xuan, Y.; Feng, J.; Tang, Z.; Li, Y.; Wang, L. Influence of start-up modes on the noise characteristics of mixed-flow pump during start-up process. *Mech. Syst. Signal Process.* **2024**, *214*, 111388. [CrossRef]
16. Tang, Z.; Zhu, G.; Feng, J.; Wu, Y.; Liu, K.; Lu, Q. Influence of pump start-up mode on the stability of mixed-flow pumps. *J. Mech. Sci. Technol.* **2023**, *37*, 2949–2958. [CrossRef]
17. Li, H.; Bai, C.; Wang, J. Experiments and numerical analysis of the dynamic flow characteristics of a pump−pipeline system with entrapped air during start-up. *Eng. Appl. Comput. Fluid Mech.* **2023**, *17*, 2238853. [CrossRef]
18. Abdulkhaev, Z.E.; Abdurazaqov, A.M.; Sattorov, A.M. Calculation of the transition processes in the pressurized water pipes at the start of the pump unit. *JournalNX* **2021**, *7*, 285–291.
19. Devolder, B.; Troch, P.; Rauwoens, P. Performance of a buoyancy-modified k-ω and k-ω SST turbulence model for simulating wave breaking under regular waves using OpenFOAM®. *Coast. Eng.* **2018**, *138*, 49–65. [CrossRef]
20. Wang, C.; Sun, M.; Yang, Y.; Wang, H.; Liu, X.; Xiong, D.; Wang, Y. Improved SST turbulence model for supersonic flows with APG/separation. *Comput. Fluids* **2024**, *274*, 106237. [CrossRef]
21. Iovănel, R.G.; Dunca, G.; Cervantes, M.J. Study on the accuracy of RANS modelling of the turbulent flow developed in a kaplan turbine operated at BEP. Part 2—Pressure fluctuations. *J. Appl. Fluid Mech.* **2019**, *12*, 1463–1473. [CrossRef]
22. Smirnov, P.E.; Menter, F.R. Sensitization of the SST Turbulence Model to Rotation and Curvature by Applying the Spalart–Shur Correction Term. *J. Turbomach.* **2009**, *131*, 041010. [CrossRef]
23. Huang, X.; Yang, W.; Li, Y.; Qiu, B.; Guo, Q.; Zhuqing, L. Review on the sensitization of turbulence models to rotation/curvature and the application to rotating machinery. *Appl. Math. Comput.* **2018**, *341*, 46–69. [CrossRef]
24. Liu, C.; Gao, Y.-S.; Dong, X.-R.; Wang, Y.-Q.; Liu, J.-M.; Zhang, Y.-N.; Cai, X.-S.; Gui, N. Third generation of vortex identification methods: Omega and Liutex/Rortex based systems. *J. Hydrodyn.* **2019**, *31*, 205–223. [CrossRef]
25. Liu, C.; Wang, Y.; Yang, Y.; Duan, Z. New omega vortex identification method. *Sci. China Phys. Mech. Astron.* **2016**, *59*, 1–9. [CrossRef]
26. Zhou, L.; Hang, J.; Bai, L.; Krzemianowski, Z.; El-Emam, M.A.; Yasser, E.; Agarwal, R. Application of entropy production theory for energy losses and other investigation in pumps and turbines: A review. *Appl. Energy* **2022**, *318*, 119211. [CrossRef]
27. Kock, F.; Herwig, H. Local entropy production in turbulent shear flows: A high-Reynolds number model with wall functions. *Int. J. Heat Mass Transf.* **2004**, *47*, 2205–2215. [CrossRef]

28. *DIN EN ISO 9906*; Rotodynamic Pumps—Hydraulic Performance Acceptance Tests—Grades 1, 2 and 3 (ISO 9906: 2012). German Version EN ISO. Afnor Publishing: Saint-Denis, France, 2012.
29. Lilly, J.M.; Olhede, S.C. Generalized morse wavelets as a superfamily of analytic wavelets. *IEEE Trans. Signal Process.* **2012**, *60*, 6036–6041. [CrossRef]